Atmospheric Variability Drives Anomalies in the Bering Sea Air–Sea Heat Exchange

EMILY E. HAYDEN,[a] LARRY W. O'NEILL,[a] AND SETH F. ZIPPEL[a]

[a] *College of Earth, Ocean, and Atmospheric Sciences, Oregon State University, Corvallis, Oregon*

(Manuscript received 22 February 2024, in final form 28 August 2024, accepted 27 September 2024)

ABSTRACT: High latitudes, including the Bering Sea, are experiencing unprecedented rates of change. Long-term Bering Sea warming trends have been identified, and marine heatwaves (MHWs), event-scale elevated sea surface temperature (SST) extremes, have also increased in frequency and longevity in recent years. Recent work has shown that variability in air–sea coupling plays a dominant role in driving Bering Sea upper-ocean thermal variability and that surface forcing has driven an increase in the occurrence of positive ocean temperature anomalies since 2010. In this work, we characterize the drivers of the anomalous surface air–sea heat fluxes in the Bering Sea over the period 2010–22 using ERA5 fields. We show that the surface turbulent heat flux dominates the net surface heat flux variability from September to April and is primarily a result of near-surface air temperature and specific humidity anomalies. The airmass anomalies that account for the majority of the turbulent heat flux variability are a function of wind direction, with southerly (northerly) wind advecting anomalously warm (cool), moist (dry) air over the Bering Sea, resulting in positive (negative) surface turbulent flux anomalies. During the remaining months of the year, anomalies in the surface radiative fluxes account for the majority of the net surface heat flux variability and are a result of anomalous cloud coverage, anomalous lower-tropospheric virtual temperature, and sea ice coverage variability. Our results indicate that atmospheric variability drives much of the Bering Sea upper-ocean temperature variability through the mediation of the surface heat fluxes during the analysis period.

SIGNIFICANCE STATEMENT: A long-term ocean warming trend and a recent increase in marine heatwaves in the Bering Sea have been identified. Previous work showed that anomalies in the exchange of heat between the ocean and the atmosphere were the primary driver of Bering Sea temperature variability, but the processes responsible for the heat exchange anomalies were unknown. In this work, we show that the atmosphere is the primary driver of anomalies in the Bering Sea air–sea heat exchange and therefore plays an important role in altering the thermal state of the Bering Sea. Our results highlight the importance of understanding more about how the ocean and the atmosphere interact at high latitudes and how this relationship will be affected by future climate change.

KEYWORDS: North Pacific Ocean; Mesoscale processes; Atmosphere-ocean interaction; Air-sea interaction; Climate variability; Anomalies

1. Introduction

Large-scale atmospheric circulation and basin-scale sea surface temperature (SST) variability are strongly coupled in the North Pacific. On monthly to seasonal time scales, basin-scale SST anomalies (SSTAs) and atmospheric circulation anomalies covary (Wallace et al. 1990; Cayan 1992a), with the strongest air–sea coupling occurring when atmospheric forcing is driving an ocean temperature response (Cayan 1992a). The impact of atmospheric forcing on SST is maximized in boreal winter when the surface turbulent heat fluxes are at their peak (Cayan 1992a). During this time, anomalies in the air–sea temperature (humidity) difference in the presence of high mean wind speeds account for most of the variability in the sensible (latent) heat flux (Cayan 1992b). A similar, large-scale coupling between the atmosphere and the SST occurs on synoptic time scales, with surface turbulent heat flux variability being the dominant component of the atmospheric forcing (Deser and Timlin 1997). The key role of atmospheric variability in forcing basin-scale SSTA is well described on weekly to seasonal time scales, but the role of the atmosphere in driving smaller-scale ocean temperature variability in the Bering Sea, a marginal sea of the high-latitude North Pacific and the focus of this analysis (Fig. 1a), remains unclear. In a recent paper (Hayden and O'Neill 2024), we showed that anomalies in the net surface heat flux were responsible for most of the observed mixed-layer temperature anomalies (MLTa) in the Bering Sea during the period 2010–17; however, the processes driving the flux anomalies remain unknown. Upper-ocean temperature anomalies in the Bering Sea vary on a continuous spectrum of time scales, including approximately decadal (Wooster and Hollowed 1995; Danielson et al. 2020). Prior to 2010, surface and subsurface temperature anomalies displayed pronounced interannual variability that does not exceed ±2°C, through multiple phases of the Pacific decadal oscillation (PDO) (Fig. 1b). Since 2010, temperature anomalies have regularly exceeded 2°C and have remained elevated through multiple phase changes in the PDO. The goal of the present study is to determine the specific processes driving anomalies in the surface heat exchange.

Marine heatwaves (MHWs) are a component of Bering Sea temperature variability that is receiving increased attention in recent years. MHWs are relatively extreme SSTA (Hobday et al. 2016) that have increased in frequency, intensity, and spatial extent across the globe (Scannell et al. 2016), a trend

Corresponding author: Emily E. Hayden, haydenem@oregonstate.edu

DOI: 10.1175/JCLI-D-24-0105.1

© 2024 American Meteorological Society. This published article is licensed under the terms of the default AMS reuse license. For information regarding reuse of this content and general copyright information, consult the AMS Copyright Policy (www.ametsoc.org/PUBSReuseLicenses).

Brought to you by OREGON STATE UNIVERSITY | Unauthenticated | Downloaded 07/15/25 06:23 PM UTC

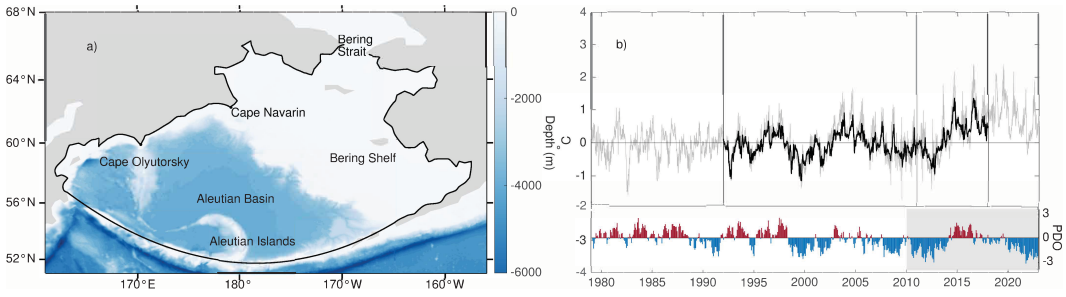

FIG. 1. (a) Map of key geographical locations in the Bering Sea, with bathymetry noted by blue shading. The study area of this analysis is outlined in black and extends from the Aleutian Islands in the south to the Bering Strait in the north. (b) Time series of area-averaged daily Bering Sea ERA5 SSTA 1979–2022 (gray) and ECCO MLTa 1992–2017 (black). The climatological base periods used to compute these anomalies are noted by vertical lines, with 1979–2010 (gray vertical lines) used for computing SSTA and the full ECCO record length of 1992–2017 (black vertical lines) used for MLTa. The sign and magnitude of the monthly PDO index over 1979–2022 are shown in the lower-right corner, with 2010–22 noted by the gray shading.

that is projected to continue with ongoing climate change (Frölicher et al. 2018). Exceptionally intense and persistent MHWs occurred in the North Pacific in 2014/15 (Di Lorenzo and Mantua 2016) and again in 2019 (Amaya et al. 2020). The precise mechanisms driving these MHWs are an area of ongoing research, but anomalous atmospheric forcing was responsible for their formation and preservation (Bond et al. 2015; Di Lorenzo and Mantua 2016; Amaya et al. 2020; Chen et al. 2023) as well as for their demise (Phillips and O'Neill 2020). These periods of persistent, elevated ocean temperatures have wide-ranging ecosystem impacts across multiple trophic levels (Cheung and Frölicher 2020; Piatt et al. 2020; Suryan et al. 2021; Wyatt et al. 2022). The Bering Sea has not been immune to this trend, with MHWs increasing in both frequency and persistence since 2010 (Carvalho et al. 2021). Similar to the North Pacific, Bering Sea MHWs have extensive ecosystem impacts (Siddon et al. 2020). The 2018/19 Bering Sea MHW was implicated as a key factor in the collapse of the snow crab fishery in 2021 (Szuwalski et al. 2023) and negatively impacted various other species, including salmon, seabird, and seal populations (Siddon et al. 2020). The extensive and deleterious impacts of MHWs on Bering Sea ecosystems, and the projected amplification of their impacts under continued climate change (Cheung and Frölicher 2020), indicate the urgency of identifying the processes that drive Bering Sea temperature extremes.

Surface forcing is the dominant driver of seasonal variability in Bering Sea upper-ocean heat content (Reed 2003; Wirts and Johnson 2005). Strong solar insolation is the primary surface forcing term during the spring and summer over both the shallow eastern shelf (Reed and Stabeno 2002; Reed 2003) and over the Aleutian basin (Wirts and Johnson 2005). During the fall and winter, the turbulent heat flux is the leading surface forcing term, as winter storms drive increased latent and sensible heat losses to the atmosphere (Reed 2003; Wirts and Johnson 2005). These previous studies established the importance of the air–sea heat exchange in driving seasonality in the Bering Sea ocean temperature state, but they were not diagnostic of the specific processes driving seasonal flux variability. Specifically, the surface turbulent heat flux anomalies could be caused by anomalies in wind speed, surface air temperature and specific humidity, and/or SST, none of which were conclusively identified as the driver. Furthermore, these previous studies were limited in space and time by available data, typically focusing on either the eastern shelf or the western basin.

In this work, we quantify the role of atmospheric variability in observed Bering Sea net surface heat flux anomalies, which we previously identified as the dominant driver of upper-ocean temperature variability (Hayden and O'Neill 2024). We examine the period 2010–22, which is coincident with a period of intense climate extremes, including the lowest sea ice extent on record (Stabeno and Bell 2019); an increased incidence of MHWs (Carvalho et al. 2021); a shift in the response of Bering Sea upper-ocean temperature to decadal variability (Fig. 1b); and the initiation of a period of increased upper-ocean warming driven by surface forcing anomalies (Hayden and O'Neill 2024). We characterize the relationship between the atmospheric state and the air–sea heat flux variability using the fifth major global reanalysis produced by European Centre for Medium-Range Weather Forecasts (ECMWF) (ERA5), emphasizing the seasonal evolution of the heat flux terms and their influence on the annual heating cycle. Our analysis provides insight into the contribution of surface forcing anomalies to temperature variability in the Bering Sea over the recent decade. The results of this work improve our fundamental understanding of air–sea interactions at high latitudes, which is relevant to the advancement of weather and ocean predictive capabilities. Increased knowledge of the role of coupled ocean–atmosphere processes in climate extremes is essential for the development of improved coupled ocean–atmosphere models. Data and methodology are described in section 2. Results are presented in section 3. A discussion of the results and their interpretation, as well as conclusions, is presented in section 4.

2. Data and methodology

a. Data

Variability in the net surface heat exchange is assessed using ERA5 fields. ERA5 is a global estimate of atmospheric state

Brought to you by OREGON STATE UNIVERSITY | Unauthenticated | Downloaded 07/15/25 06:23 PM UTC

variables at hourly intervals from 1979 to the present, on a uniform 0.25° spatial grid (Hersbach et al. 2020). Surface heat flux variables are presented as hourly averages, while other variables [i.e., ocean skin temperature T_s, 2 m air temperature T_a, 2 m air specific humidity q_a, and 10 m u and v winds] are instantaneous values at the top of each hour, and SST is a daily mean field. The surface turbulent heat flux Q_{THF} and surface upward longwave radiative flux $Q_{\mathrm{LW}\uparrow}$ are computed using the skin temperature T_s, which varies throughout the day and also differs from SST as a cool-skin and warm-layer correction is applied to account for temperature differences within the top few meters of the surface. The skin temperature is the ocean temperature variable used to compute the surface heat fluxes in the ERA5 reanalysis system.

ERA5 was chosen over other reanalysis products primarily because of its high temporal and spatial resolution (Hersbach et al. 2020), as well as its performance in capturing variables of interest. ERA-Interim, the precursor to ERA5, was one of the best-performing reanalysis products in comparison with in situ estimates of the surface turbulent heat fluxes in the Bering Sea (Kong et al. 2019). Assessments of the performance of ERA5 in other North Pacific and Arctic regions suggest it is one of the best available data products for our analysis, because of its ability to reproduce independent observations of the surface turbulent heat fluxes (Phillips and O'Neill 2020; Renfrew et al. 2021), other key meteorological variables (Graham et al. 2019) used in this work, and the net surface radiative flux (Seo et al. 2020). Over the global ocean, satellite-based observations of the downward longwave radiative flux $Q_{\mathrm{LW}\downarrow}$ performed slightly better (RMSE = 11.6 W m^{-2}) than ERA5 (RMSE = 12.5 W m^{-2}) in comparison with observations, but ERA5 had the lowest RMSE relative to other reanalysis products (Feng et al. 2023).

Sea ice plays an important role in the climate of the Bering Sea (Overland 1981). Interactions between the atmosphere, ocean, and sea ice drive physical variability in the region (Stabeno et al. 1999). Sea ice concentration is not generated as a prognostic or forecast field in ERA5; rather, it is a specified surface boundary condition comprised of a combination of the daily ECMWF OCEAN5 reanalysis and the Met Office Operational SST and Sea Ice Analysis (OSTIA) (IFS Documentation–Part II 2023).

We used daily mean ERA5 fields of the net surface heat fluxes, the clear-sky (CS) net surface radiative fluxes, sea ice concentration, 10-m winds, geopotential height, cloud fraction, T_s, T_a, and q_a. The net air–sea heat flux Q_{net} is the sum of the turbulent heat flux Q_{THF} [sensible heat flux Q_{SH} plus latent heat flux Q_{LH}] and the net radiative flux Q_{RAD} [net shortwave radiative flux Q_{SW} plus net longwave radiative flux Q_{LW}]:

$$Q_{\mathrm{net}} = Q_{\mathrm{SH}} + Q_{\mathrm{LH}} + Q_{\mathrm{SW}} + Q_{\mathrm{LW}}. \quad (1)$$

Following the ECMWF convention for surface fluxes, positive values of Q_{net} and each component term in Eq. (1) indicate a downward (ocean warming) heat flux and vice versa. The terms Q_{SW} and Q_{LW} can be separated into their upwelling ↑ and downwelling ↓ components so that Q_{net} is

$$Q_{\mathrm{net}} = Q_{\mathrm{SH}} + Q_{\mathrm{LH}} + Q_{\mathrm{SW}\downarrow} + Q_{\mathrm{SW}\uparrow} + Q_{\mathrm{LW}\downarrow} + Q_{\mathrm{LW}\uparrow}. \quad (2)$$

We computed the upwelling components of Q_{SW} and Q_{LW} as the difference between the relevant net surface radiative term and the downwelling terms. We recognize that upward shortwave radiative flux $Q_{\mathrm{SW}\uparrow}$ is a function of downward shortwave radiative flux $Q_{\mathrm{SW}\downarrow}$ and the surface albedo, but we have elected to consider them as separate terms because of the possibility of small amounts of sea ice driving a large upward flux anomaly.

In section 4, we also consider a metric for determining a reference SST response to a given surface flux forcing. To do so, we used the NASA/JPL Estimating the Circulation and Climate of the Ocean (ECCO) Version 4 Release 4 (V4r4) Ocean State and Sea Ice Estimate (Fukumori et al. 2017; ECCO Consortium et al. 2021) fields of mixed-layer depth (MLD) h, available for 1992–2017. The term h is provided on a Lat-Lon-Cap 90 (LLC90), nonuniform grid, which corresponds to horizontal grid sizes of approximately 60 km in the Bering Sea (Forget et al. 2015).

b. Climatologies and anomalies

Daily mean climatological values for all ERA5 fields were computed relative to the base period 1979–2010, resulting in 366-day-long fields for each variable and denoted by overbars throughout this work. Daily anomalies relative to the climatological base period, denoted by primes, were computed as

$$F'(i, j, t) = F(i, j, t) - \overline{F}(i, j), \quad (3)$$

where F is the daily variable of interest, i corresponds to gridpoint latitude, j corresponds to gridpoint longitude, and t corresponds to the time in days. We chose the base period of 1979–2010 to align with the climatological base period used by other assessments of recent variability and anomalies in the Bering Sea (i.e., Danielson et al. 2020; Carvalho et al. 2021; Baker et al. 2020), which allows us to contextualize our results in the existing literature. Furthermore, we found that our results were not sensitive to the chosen base period (not shown) principally because sea ice significantly attenuates energy exchange between the ocean and the atmosphere.

c. Sea ice masking

At high latitudes, sea ice complicates our understanding of the air–sea heat exchange, as both the air–sea heat fluxes and sea ice display high seasonal variability, making their impact on Bering Sea temperature difficult to separate. Furthermore, our understanding of the annual cycle of the surface heat fluxes over sea ice is incomplete, largely due to inadequate measurements (Bourassa et al. 2013). Because heat fluxes over the sea ice and their seasonal variability are not yet fully understood, and because they are fundamentally different from the air–sea fluxes, we removed ERA5 grid cells containing sea ice in our analysis.

To determine a suitable "metric" for our sea ice mask, we evaluated the effect of masking ice-covered grid cells using: 1) a sea ice extent criterion of grid cells covered by ≥15% sea

Brought to you by OREGON STATE UNIVERSITY | Unauthenticated | Downloaded 07/15/25 06:23 PM UTC

TABLE 1. Total number of joules contributed by daily mean ERA5 net surface heat flux anomalies Q'_{net}, the total number of joules contributed when a 15% sea ice coverage ice mask is applied, and when a fractional ice mask coverage is applied. The total energy exchange was computed by integrating over the Bering Sea, bounded to the north by the Bering Strait and to the south by the Aleutian Islands (Fig. 1a), over 2010–22.

Q'_{net}	15% mask	Fractional mask
4.084×10^{21}	4.201×10^{21}	3.948×10^{21}

ice concentration and 2) a fractional ice mask that weighted the heat flux per grid cell according to the fraction of the grid cell covered by sea ice. We compared the total number of joules entering the Bering Sea over 2010–22 for the unmasked net air–sea heat flux anomaly Q'_{net} fields, to the total number of joules associated with each ice mask metric (Table 1). The 15% sea ice concentration criterion preserved most of the variability in the Q'_{net}, with the total number of joules differing by <3% from the unmasked fields. In addition, the 15% coverage criterion aligns with the commonly used threshold for sea ice extent in a grid cell (ECMWF 2019; Matthews et al. 2020; Meier et al. 2021). Because of the apparent small differences in net air–sea heat exchange, we chose the common definition of 15% sea ice fraction for our ice mask, and hereafter, all grid cells with ≥15% sea ice fraction in all variables are removed from the analysis.

By masking sea ice, there will be a different number of data points available for different grid cells, due to the seasonality and spatial extent of sea ice (Fig. 2). We recognize that this processing choice results in a small sampling bias, but argue that it is necessary to focus on air–sea interactions only, rather than confounded air–sea and air–sea ice interactions. The impact of our treatment of sea ice on our results is reviewed in the discussion section.

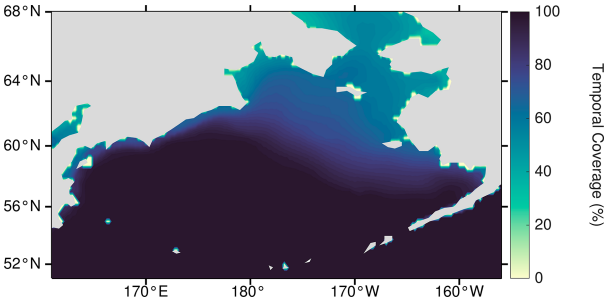

FIG. 2. Temporal coverage of all fields at each grid cell, 2010–22, computed as the percentage of available data points relative to the total record length, after grid cells containing ≥15% sea ice coverage are removed.

d. Balance metric

We implement the balance metric M_B approach of Halkides et al. (2015) to assess spatial variability in the seasonally varying heat flux anomaly terms [Eq. (1)]. The term M_B, defined as

$$M_B(P_1, P_2, T_t) \equiv \frac{\langle (P_2 - T_t)^2 \rangle - \langle (P_1 - T_t)^2 \rangle}{\langle (P_2 - T_t)^2 \rangle + \langle (P_1 - T_t)^2 \rangle} \begin{cases} 0 < M_B \le +1 & P_1 \text{ is more important} \\ M_B = 0 & P_1 \text{ and } P_2 \text{ contribute equally} \\ 0 > M_B \ge -1 & P_2 \text{ is more important} \end{cases}, \quad (4)$$

describes the relative importance of two forcing processes P_1 and P_2 in driving spatial variability in a mixed layer tracer tendency response term T_t, with angle brackets indicating ensemble averaging over time. We define the net radiative flux anomaly Q'_{RAD} as P_1, the turbulent heat flux anomaly Q'_{THF} as P_2, and Q'_{net} as T_t. Because Q'_{net} is fully described by the sum of Q'_{THF} and Q'_{RAD} and is thus a closed budget [Eq. (1)], analysis of M_B fully describes the sources of variability of Q'_{net} among the surface turbulent and net radiative heat fluxes. When $M_B = -1$, Q'_{THF} accounts for all of the variance of Q'_{net}, and when $M_B = 1$, Q'_{RAD} accounts for all Q'_{net} variance. When $M_B = 0$, the variance of Q'_{net} is equally partitioned between Q'_{THF} and Q'_{RAD}.

e. Cloud radiative forcing

To assess the role of cloud coverage variability in anomalous Bering Sea air–sea heat exchange, we computed cloud radiative forcing (CRF) components (Ramanathan et al. 1989; Shupe and Intrieri 2004) and their anomalies for Q_{RAD}, Q_{LW}, Q_{SW}, and their upwelling and downwelling components. The generalized method for computing CRF is the difference between the all-sky (AS) radiative flux and the CS radiative flux:

$$Q_{RAD_{CRF}} = Q_{RAD_{AS}} - Q_{RAD_{CS}}, \quad (5)$$

where the CS fields are computed in the absence of clouds and provided as part of the ERA5 data collection. The cloud radiative fluxes computed in this fashion are a function of only cloud properties. Following the ECMWF convention for the sign of the radiative fluxes, when CRF is positive, clouds warm the surface relative to the clear sky, and when it is negative, clouds cool the surface relative to the clear sky.

f. Potential mixed-layer heating terms

We estimated potential mixed-layer heating rate terms that describe the possible impact of Q'_{net} on the Bering Sea MLT, in the absence of oceanic heat advection and diffusion. These terms are not descriptive of a closed ocean mixed-layer heat budget; rather, they describe the potential impact of the

Brought to you by OREGON STATE UNIVERSITY | Unauthenticated | Downloaded 07/15/25 06:23 PM UTC

observed air–sea heat flux anomalies on the ocean thermal state if all of the anomalous surface heating went into changing MLT, while accounting for the effect of the seasonally varying MLD on the ocean temperature response to a given surface forcing. Changes in the vertically averaged ocean MLT T_m over a given time can be described by an MLT tendency equation (e.g., Frankignoul 1985; Phillips and O'Neill 2020). An abbreviated version, used in Hayden and O'Neill (2024), is given by

$$\frac{\partial T_m}{\partial t} = \frac{\partial T_{\mathrm{SF}}}{\partial t} + \frac{\partial T_{\mathrm{OD}}}{\partial t}, \tag{6}$$

where the first term on the right-hand side describes the MLT response to the net air–sea heat flux [Eq. (1)]. The second term is an ocean dynamic term, defined as the net effect of vertical and horizontal advection, entrainment, and turbulent exchanges at the base of the mixed layer on MLT tendency. The potential impact of penetrative shortwave radiation leaving the mixed layer is not accounted for here, but is generally small in the Bering Sea (i.e., Fig. 1; Tian and Zhang 2023). We showed previously (Hayden and O'Neill 2024) that surface forcing variability ($\partial T_{\mathrm{SF}}/\partial t$) accounted for more than 70% of the variability in the Bering Sea MLT tendency anomalies (1992–2017). Therefore, we argue that focusing only on the surface forcing term in Eq. (6) can provide significant insight into Bering Sea MLT variability, even though the contribution from the neglected ocean dynamics is still $\mathcal{O}(1)$. We evaluated the daily potential heating rate due to anomalies in Q'_{net} and each term in Eq. (2) according to

$$\frac{\partial T'_{\mathrm{SF}}}{\partial t} = \frac{Q'_{\mathrm{net}}}{\rho_o C_{P_o} h} \equiv F'_{\mathrm{net}}, \tag{7}$$

where seawater density ρ_o is set equal to a constant value of 1029 kg m^{-3}, the specific heat of seawater C_{P_o} is set equal to 3993 J kg^{-1} K^{-1}, and h is the MLD. We present the potential heating rate in units of degrees Celsius per day (°C day^{-1}) throughout. Because of the differing temporal coverage of ERA5 and ECCO, we use a daily climatological (1992–2017) ECCO MLD, which is bilinearly interpolated to the 0.25° ERA5 spatial grid. Because we use a daily mean climatological value for the MLD, we are not evaluating the effect of the surface heat flux anomalies on MLD on daily time scales, nor are we assessing how variability in MLD feeds back onto the atmosphere through the net surface fluxes. We estimated the first-order sensitivity of the potential heating rate to the use of a climatological MLD as

$$\delta F'_{\mathrm{net}} = \left|\frac{\partial F'_{\mathrm{net}}}{\partial h}\right| \sigma_h, \tag{8}$$

where σ_h is the interannual variability of the daily MLD at each grid cell, computed from daily ECCO fields for 1992–2017. We found that $\delta F'$ was on the order of 10^{-1} °C day^{-1} and thus only had a small effect on mixed-layer temperature variability.

g. Heat flux decomposition

A primary goal of this work is to diagnose the specific drivers of the various net surface heat flux terms [Eq. (1)]. The turbulent heat fluxes in ERA5 are computed using a nonlinear system of equations based on the Monin–Obukhov similarity theory, and thus, isolating the drivers of flux anomalies is not possible from the ERA5 fields. We developed a strategy for diagnosing the drivers through the estimation of the ERA5 latent and sensible heat flux anomalies using a simple approximation of the turbulent heat fluxes. To determine the role of air temperature, ocean temperature, air humidity, and wind speed in driving anomalies in Q_{THF}, we first estimated Q_{SH} and Q_{LH} by their bulk aerodynamic formulation and then computed a decomposition of the sensible heat flux anomaly Q'_{SH} and latent heat flux anomaly Q'_{LH} in terms of their climatological mean and anomaly components in a fashion similar to, for instance, Tanimoto et al. (2003). A detailed derivation is shown in the appendix. Briefly, estimates of ERA5 fields of Q'_{SH} and Q'_{LH}, denoted by $\tilde{Q}'_{\mathrm{SH}}$ and $\tilde{Q}'_{\mathrm{LH}}$, were estimated using standard bulk formulas as

$$\tilde{Q}'_{\mathrm{SH}} = \rho_a C_P C_H \Big(\underbrace{\overline{V}\Delta T'}_{1} + \underbrace{V'\overline{\Delta T}}_{2} + \underbrace{V'\Delta T'}_{3} \Big), \tag{9}$$

$$\tilde{Q}'_{\mathrm{LH}} = \rho_a C_Q L_V \Big(\underbrace{\overline{V}\Delta q'}_{1} + \underbrace{V'\overline{\Delta q}}_{2} + \underbrace{V'\Delta q'}_{3} \Big). \tag{10}$$

In both equations, primed terms denote daily anomalies, relative to the 1979–2010 daily climatology, and overbars denote daily climatological mean values (1979–2010) [Eq. (3)]. The term V is the wind speed 2 m above the surface, computed by adjusting the 10-m wind speed using the same stability-dependent surface layer wind profile formulation used in ERA5. The term ΔT is the air–sea temperature difference $T_a - T_s$. The term Δq is the air–sea specific humidity difference $q_a - q_s$. The term T_s is the ERA5 skin temperature, and q_s is the sea surface saturation specific humidity computed from T_s. Daily climatological fields of air density ρ_a were used in both equations. We assume constant air specific heat capacity C_P = 1025 J kg^{-1} K^{-1}, for $\tilde{Q}'_{\mathrm{SH}}$, and a constant latent heat of vaporization $L_V = 2.5 \times 10^{-6}$ J kg^{-1}, for $\tilde{Q}'_{\mathrm{LH}}$. Because ERA5 does not output the transfer coefficients C_H and C_Q we computed daily fields of C_H and C_Q according to Eqs. (3.17) and (3.18) in IFS Documentation–Part IV (2023), using ERA5 fields of momentum roughness length, and an Obukhov length estimated using a buoyancy flux estimated from Q_{SH} and Q_{LH} as per IFS Documentation–Part IV (2023). Although C_H and C_Q vary with wind speed (and to a lesser degree, temperature, and humidity), we did not decompose the transfer coefficients into their mean and climatological components, as we are primarily interested in variability in the atmosphere and in ocean surface temperature and their role in driving Q'_{THF}. The mean contribution of the covarying anomaly terms $\overline{V'\Delta T'}$ and $\overline{V'\Delta q'}$ is negligible loss terms that do not significantly contribute to the performance of the decompositions and are not included here. To assess the validity of our decompositions, we compared them to the equivalent ERA5 Q'_{SH} and Q'_{LH} fields. Our approximate turbulent flux anomaly decompositions display good agreement with the ERA5 surface flux anomalies (Figs. 3a,b). The RMS difference between $\tilde{Q}'_{\mathrm{SH}}$ and $\tilde{Q}'_{\mathrm{LH}}$ and their respective ERA5

Brought to you by OREGON STATE UNIVERSITY | Unauthenticated | Downloaded 07/15/25 06:23 PM UTC

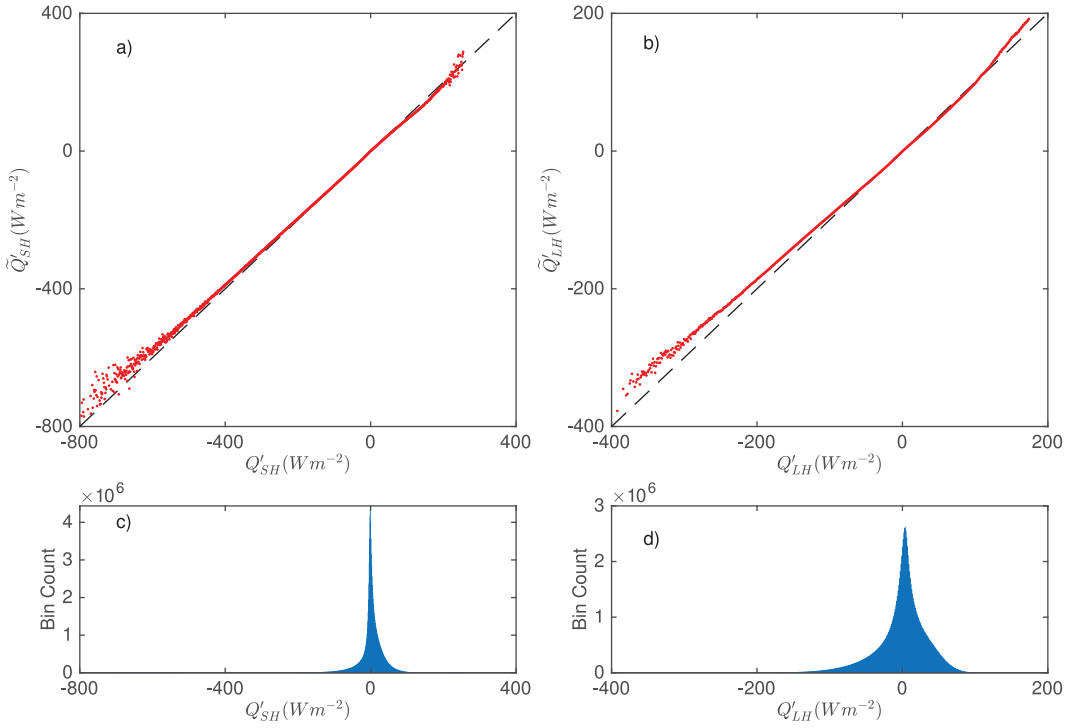

FIG. 3. (a) Bin mean of the approximate $\tilde{Q}'_{\mathrm{SH}}$ [Eq. (9)] (y axis) computed as a function of ERA5 Q'_{SH} (x axis). (b) Bin mean of the approximate $\tilde{Q}'_{\mathrm{LH}}$ [Eq. (10)] (y axis) computed as a function of ERA5 Q'_{LH} (x axis). A bin width of 1 W m^{-2} was used for both (a) and (b). (c),(d) Histograms showing the density of points within the bins shown in (a) and (b), respectively. All data presented here are daily means for each grid point over the spatial domain shown in Fig. 1a, for the period 1979–2022.

fields is ~6 W m^{-2}. To estimate whether the differences are statistically significant, we performed a two-sample Kolmogorov–Smirnov test comparing the probability distribution of our decompositions against their respective ERA5 counterparts. For Q'_{SH}, $D = 0.0094$, $p < 0.001$, with a significance level of less than 1%. For Q'_{LH}, $D = 0.0182$, $p < 0.001$, with a significance level of less than 1%. Therefore, the differences between the distributions of our decomposition and their respective ERA5 fields are not statistically significant below the 99% significance level. Our decomposition slightly underestimates the ERA5 Q'_{THF} at large, negative values, likely due to our approximation of the transfer coefficients, and because our decomposition is computed using daily means of hourly instantaneous fields, while the ERA5 surface turbulent heat fluxes are averaged over hourly periods. We investigated multiple methods of estimating the transfer coefficients and found that using daily fields of C_H and C_Q resulted in the best match between the ERA5 and decomposition fields. Although the large-magnitude positive and negative flux anomalies in our decomposition were most sensitive to the choice of transfer coefficient approximations, the majority of the points that contribute to Q'_{THF} occur within a small range of values (Figs. 3c,d) that are relatively insensitive to the choice of transfer coefficient. Because $\tilde{Q}'_{\mathrm{SH}}$ and $\tilde{Q}'_{\mathrm{LH}}$ well approximate Q'_{SH} and Q'_{LH}, we proceed to use our decomposed turbulent heat flux fields to diagnose the drivers of Q'_{THF} variability.

3. Results

a. Seasonal variability of the air–sea heat flux anomalies

We quantified the seasonally varying contribution of Q'_{RAD} and Q'_{THF} to variability in Q'_{net}, by computing $M_B(Q'_{\mathrm{RAD}}, Q'_{\mathrm{THF}}, Q'_{\mathrm{net}})$ for each month of the year, using daily mean fields of the surface heat flux anomalies, and ensemble averaging the daily fields for each month (Fig. 4). Over the analysis region (Fig. 1a), Q'_{THF} accounts for, on average, ≥90% of Q'_{net} variability in January–March and ~70% in April. In April, there is a shift to an increasing contribution from Q'_{RAD}. Beginning in May, Q'_{RAD} is the dominant term over much of the Bering Sea, accounting for an average of 73% of the Q'_{net} variability, although over the shelf break there is a similar magnitude contribution from Q'_{THF}. The term Q'_{RAD} becomes increasingly important in June and July, accounting for 90% and 86%, respectively, of Q'_{net} variability. In August, there is a latitudinal gradient in the terms driving variability in Q'_{net}, with Q'_{THF} more important over the shallow, northern region and Q'_{RAD} remaining more important over the southern Bering Sea. In September, there is a transition back to the dominance of Q'_{THF} (83%) that is maximized in the north. The term Q'_{THF} continues to drive the majority of the variability in Q'_{net} in October–December, accounting for at least 94% of Q'_{net} in these months. These results indicate significant seasonal evolution in the processes contributing to variability in Q'_{net},

Brought to you by OREGON STATE UNIVERSITY | Unauthenticated | Downloaded 07/15/25 06:23 PM UTC

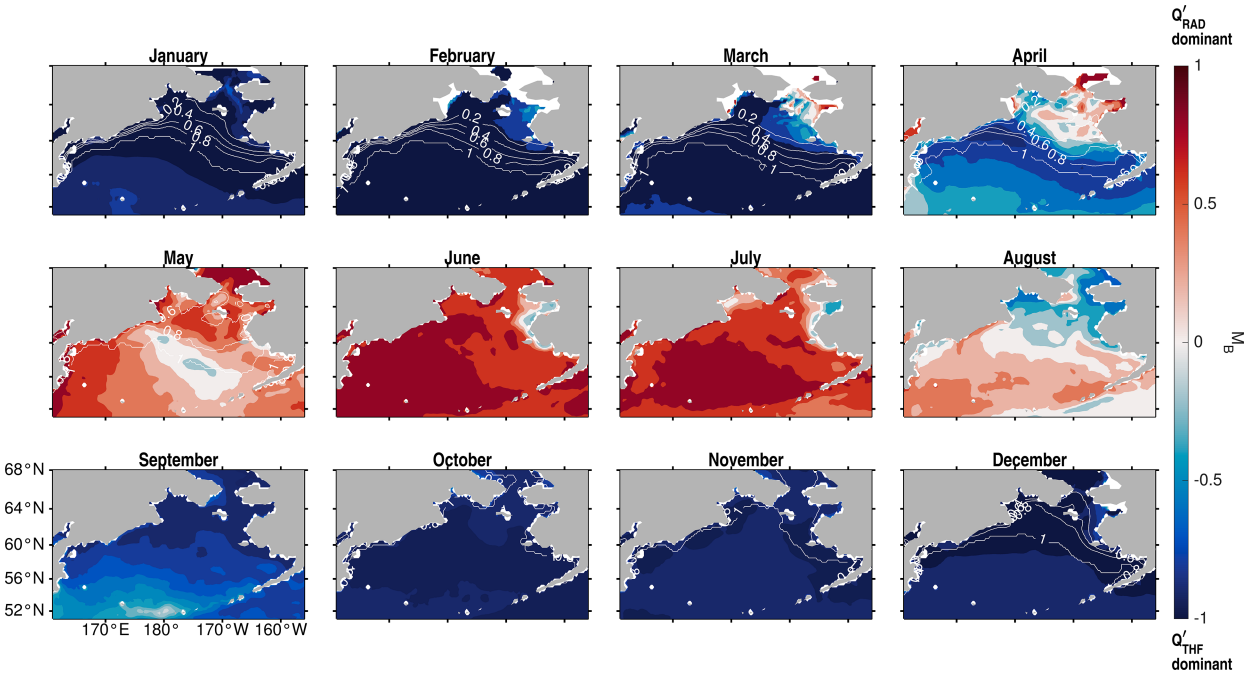

FIG. 4. Monthly balance metric $M_B(Q'_{\mathrm{RAD}}, Q'_{\mathrm{THF}}, Q'_{\mathrm{net}})$, 2010–22, comparing the role of daily ERA5 Q'_{RAD} to Q'_{THF} in driving Q'_{net}. When $M_B = 1$, Q'_{RAD} drives all of the variance in Q'_{net}; when $M_B = -1$, Q'_{THF} drives the variability; and when $M_B = 0$, the variance in Q'_{net} is equally partitioned between Q'_{THF} and Q'_{RAD}. The fraction of available data points relative to the total record length for that month is shown by the white contour lines. The contours are only plotted during months when sea ice coverage results in a reduction in the number of available data points in the Bering Sea, south of the Bering Strait.

motivating us to characterize these processes in the next two sections.

b. *Diagnosing the drivers of surface turbulent heat flux variability*

Anomalies in the surface turbulent heat fluxes account for the majority of Q'_{net} in September–April, and we now identify the processes responsible for Q'_{THF}. Returning to the bulk flux representation of the sensible [Eq. (9)] and latent [Eq. (10)] heat fluxes, it is clear that Q'_{SH} and Q'_{LH} could result from variability in the ocean skin temperature, surface air temperature, surface humidity, wind speed, or covarying combinations of these variables. In this section, we identify which state variables are driving Q'_{THF}, identifying key processes responsible for turbulent heat flux anomalies in the Bering Sea.

1) THE ROLE OF THE ATMOSPHERE IN DRIVING TURBULENT HEAT FLUX ANOMALIES

We assess the relative contribution of each term in $\tilde{Q}'_{\mathrm{SH}}$ [Eq. (9)] and $\tilde{Q}'_{\mathrm{LH}}$ [Eq. (10)] using dominance analysis (DA) techniques (Budescu 1993; Azen and Budescu 2003), which were described in detail in Hayden and O'Neill (2024). Briefly, DA is a linear regression technique that partitions the variance in a field, in this case $\tilde{Q}'_{\mathrm{SH}}$ and $\tilde{Q}'_{\mathrm{LH}}$, among each of their component terms [right-hand side of Eqs. (9) and (10), respectively]. Its strength lies in the fact that DA determines which component variable contributes most to the variance of the surface flux anomaly, after accounting for all other predictors and their cross covariances. The average variance described by a term is computed as a spatial average over the region indicated in Fig. 1a.

Anomalies in the air–sea temperature difference $\Delta T'$ [term 1 in Eq. (9)] are the dominant driver of $\tilde{Q}'_{\mathrm{SH}}$ variability in September–April, describing an average of 73% of its variance (Fig. 5a). The maximum variance described by this term (90%) occurs over the deep basin, reaching a minimum of 65% over the shelf. Wind speed anomalies V' [term 2 in Eq. (9); Fig. 5b] and covarying anomalies in V and ΔT [term 3 in Eq. (9); Fig. 5c] account for an average of 10% and 17%, respectively, of $\tilde{Q}'_{\mathrm{SH}}$ variability. The maximum variance described by V' occurs near Cape Olyutorsky (25%), with a minimum value of 6% off the coast of Alaska. The $V'\Delta T'$ minimum of 10% occurs over the deep basin, and its maximum of 25% occurs over the eastern shelf. Because anomalies in the ΔT term account for the majority of $\tilde{Q}'_{\mathrm{SH}}$ variability, we separated term 1 in Eq. (9) into contributions from 2-m air temperature anomalies T'_a and ocean skin temperature anomalies T'_s:

$$\rho_a C_P C_H \overline{V}\Delta T' = \rho_a C_P C_H \Big(\underbrace{\overline{V}T'_a}_{a} - \underbrace{\overline{V}T'_s}_{b} \Big). \tag{11}$$

This decomposition allows the determination of whether the sensible heat flux anomalies are driven by oceanic or atmospheric variability. Anomalies in the air temperature [term a in Eq. (11)] account for an average of 89% of the variance in term 1 of $\tilde{Q}'_{\mathrm{SH}}$ (Fig. 5d), with a maximum value of 97% over

Brought to you by OREGON STATE UNIVERSITY | Unauthenticated | Downloaded 07/15/25 06:23 PM UTC

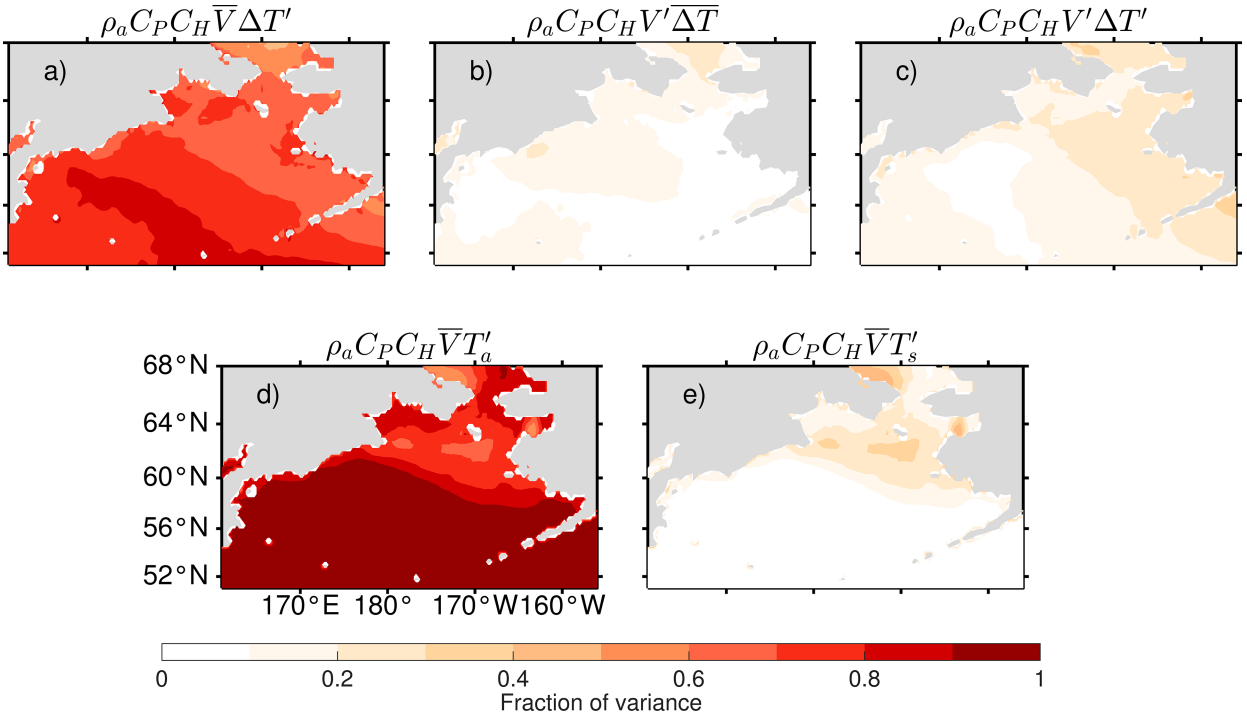

FIG. 5. (a)–(c) Fraction of the variance of the September–April daily ERA5 sensible heat flux anomaly decomposition $\tilde{Q}'_{\mathrm{SH}}$ accounted for by each term in its decomposition [Eq. (9)], computed using DA techniques. (d),(e) Fraction of the variance of term 1 in $\tilde{Q}'_{\mathrm{SH}}$ accounted for by the term proportional to T'_a and that proportional to T'_s [Eq. (11)].

much of the deep basin and a minimum value of 70% south of the Bering Strait. The term Q'_s [term b in Eq. (11)] accounts for only 11% of the variance (Fig. 5e).

The term $\tilde{Q}'_{\mathrm{LH}}$ is primarily a result of anomalies in the air–sea specific humidity difference $\Delta q'$ [term 1 in Eq. (10)], which accounts for more than 65% of its total variance (Fig. 6a), with a peak of 70% over parts of the shelf and north of the Aleutian Islands and a minimum of 60% off of the eastern coast. The term V' [term 2 in Eq. (10); Fig. 6b] accounts for over 25% of the total variance of $\tilde{Q}'_{\mathrm{LH}}$, with a minimum of 15% on the shelf and a maximum of 30% near the capes. Covarying anomalies in V and Δq [term 3 in Eq. (10); Fig. 6c] describe 9% of the total variance, with a minimum of 6% over much of the basin and southern shelf and a maximum of 15% in small patches on the shelf. Similar to $\tilde{Q}'_{\mathrm{SH}}$, term 1 in Eq. (10) was separated into contributions from air specific humidity anomalies q'_a and sea surface specific humidity anomalies q'_s:

$$\rho_a C_Q L_V \overline{V}\Delta q' = \rho_a C_Q L_V \Big(\underbrace{\overline{V} q'_a}_{a} - \underbrace{\overline{V} q'_s}_{b} \Big). \tag{12}$$

The term q'_a [term a in Eq. (12)] accounts for 91% of the variance in term 1 of $\tilde{Q}'_{\mathrm{LH}}$ (Fig. 6d), with a maximum value of 97% over most of the analysis region and a minimum of 75% near Cape Navarin. The term q'_s [term b in Eq. (12)] accounts for 9% (Fig. 6e) of the total Q'_{LH} variance, with a value of <5% over most of the Bering Sea and a maximum of 25% coincident with the area where q'_a is minimized.

These results indicate that, from 2010 to 2022, anomalies in near-surface air temperature and humidity account for the majority of the variance in the September–April Q'_{THF}, with wind speed anomalies evidently driving little of Q'_{THF}. We conclude that seasonal variability in Q_{THF} is primarily driven by atmospheric heat and moisture variability rather than ocean variability during these months. While wind speed anomalies are not significant drivers of Q'_{THF}, we show next that the wind nonetheless does play a role in producing air temperature and humidity anomalies.

2) WIND DIRECTION INFLUENCES THE SIGN AND MAGNITUDE OF TURBULENT HEAT FLUX ANOMALIES

In the previous section, we described the dominant role of near-surface air temperature and humidity anomalies in driving variability in Q'_{THF}. We now assess the role of wind direction in these airmass anomalies, to determine the contribution of atmospheric circulation to Q'_{THF}. We evaluated the relationship between wind direction θ and $\tilde{Q}'_{\mathrm{SH}}$ and $\tilde{Q}'_{\mathrm{LH}}$, and each term in their decomposition, by bin averaging the anomalous flux fields as functions of θ. For $\tilde{Q}'_{\mathrm{SH}}$ (Fig. 7a) and term 1 in its decomposition (Fig. 7b, solid curve), there is an approximately sinusoidal relationship with the wind direction. Southerly ($\theta = 180°$)-to-easterly ($\theta = 270°$) wind is associated with large positive $\tilde{Q}'_{\mathrm{SH}}$, with the component proportional to $\overline{V}\Delta T'$ [term 1 in Eq. (9)] displaying a similar relationship. Northerly ($\theta = 0°$) wind is associated with large negative $\tilde{Q}'_{\mathrm{SH}}$, with the component proportional to $\overline{V}\Delta T'$ again displaying a similar relationship.

Brought to you by OREGON STATE UNIVERSITY | Unauthenticated | Downloaded 07/15/25 06:23 PM UTC

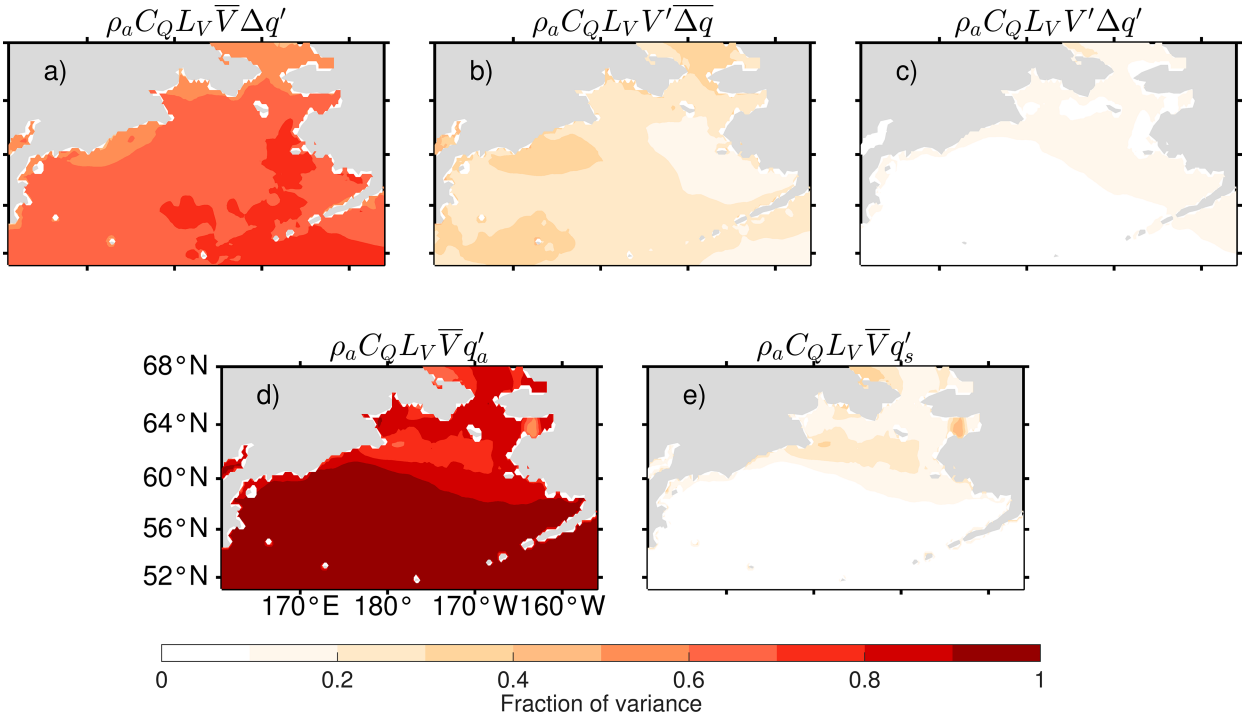

FIG. 6. (a)–(c) Fraction of the variance of the September–April daily ERA5 latent heat flux anomaly decomposition $\tilde{Q}'_{\mathrm{LH}}$ accounted for by each term in its decomposition [Eq. (10)], computed using DA techniques. (d),(e) Fraction of the variance of term 1 in $\tilde{Q}'_{\mathrm{LH}}$ accounted for by the term proportional to q'_a and that proportional to q'_s [Eq. (10)].

Westerly wind ($\theta = 90°$) is associated with a transition from negative to positive flux anomalies. As expected from the previous section, the part of term 1 in $\tilde{Q}'_{\mathrm{SH}}$ driven by T'_a [term a in Eq. (11)] accounts for the majority of $\tilde{Q}'_{\mathrm{SH}}$ and displays a similar sinusoidal relationship with θ (Fig. 7c, solid curve), while the term driven by T'_s [term b in Eq. (11)] displays no clear relationship with wind direction (Fig. 7c, dashed curve). The small amplitude of the T'_s term demonstrates that ocean skin temperature anomalies are not significant drivers of the $\tilde{Q}'_{\mathrm{SH}}$ during September–April. The remaining two terms in the decomposition of $\tilde{Q}'_{\mathrm{SH}}$ do not display a clear relationship with the wind direction (dashed and dotted curves in Fig. 7b). These results show that the atmosphere is the predominant driver of anomalous sensible heat flux on seasonal time scales.

Similar results were found for $\tilde{Q}'_{\mathrm{LH}}$ and $\overline{V}\Delta q'$ [term 1 in Eq. 10)], which both have an approximately sinusoidal relationship with wind direction (Fig. 7d and solid curve in Fig. 7e). Positive latent heat flux anomalies are associated with southerly wind and negative latent heat flux anomalies with northerly wind. The part of term 1 proportional to q'_a [term a in Eq. (12)] accounts for the majority of $\tilde{Q}'_{\mathrm{LH}}$ and displays an approximately sinusoidal relationship with wind direction (solid curve in Fig. 7f). The term proportional to q'_s [term b in Eq. (12)] does not display a strong relationship with wind direction (dashed curve in Fig. 7f). Finally, there is no clear relationship between the other two terms in the $\tilde{Q}'_{\mathrm{LH}}$ decomposition and wind direction (dashed and dotted curves in Fig. 7e). This is suggestive of southerly wind advecting anomalously humid air over the Bering Sea and driving an increase in positive $\tilde{Q}'_{\mathrm{LH}}$, through suppression of ocean heat loss by a reduction in evaporation at the ocean surface and of northerly wind advecting anomalously dry air that results in negative $\tilde{Q}'_{\mathrm{LH}}$.

3) The role of the ocean in driving summertime surface turbulent heat flux anomalies

The term Q'_{RAD} dominates the net surface heat flux anomaly signal in May–August (Fig. 4), but we evaluate the drivers of Q'_{THF} during these months nonetheless to understand seasonal variability in its drivers. The term $\tilde{Q}'_{\mathrm{SH}}$ is primarily a result of $\Delta T'$ (70% of total variance; Fig. 8a), and T'_a still accounts for most of the variance in this term of the decomposition (66%; Fig. 8d). However, the contribution from T'_s is 3 times larger in the summer (34%; Fig. 8e) in comparison with the September–April months (11%; Fig. 5e). In addition, there is a stronger contribution in May–August from covarying anomalies in V and ΔT, which now account for the 25% of total variance in $\tilde{Q}'_{\mathrm{SH}}$ (Fig. 8c). For the latent heat flux, anomalies in $\Delta q'$ remain dominant, accounting for 72% of the variance in $\tilde{Q}'_{\mathrm{LH}}$ (Fig. 9a), while the contribution from the V' is reduced (13%; Fig. 9b) and that from the covarying V and Δq anomalies is increased (15%; Fig. 9c) relative to the September–April period (Fig. 6). In addition, anomalies in q'_s contribute more to the variance (25%; Fig. 9e) in this season. These results suggest that ocean variability plays a larger role in modulating the turbulent air–sea heat exchange during May–August than during September–April.

Brought to you by OREGON STATE UNIVERSITY | Unauthenticated | Downloaded 07/15/25 06:23 PM UTC

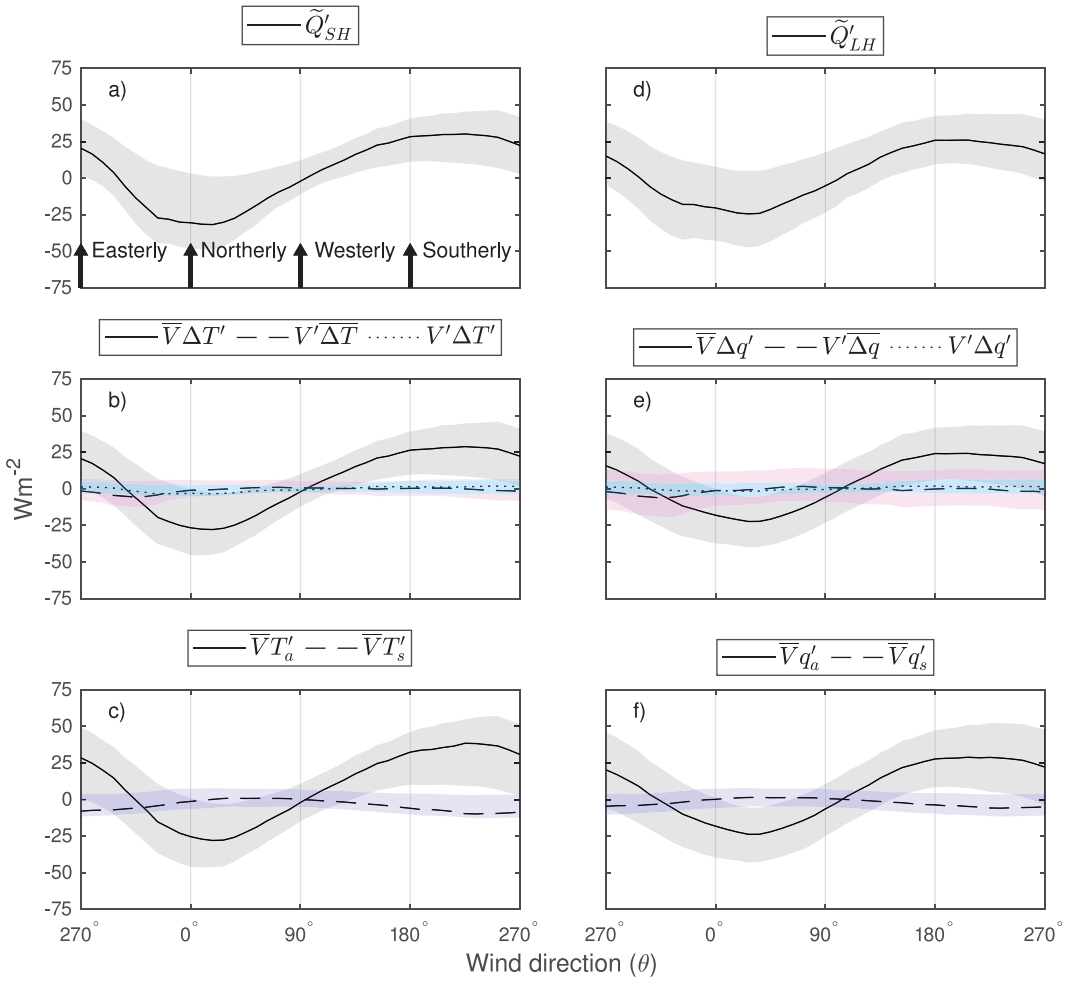

FIG. 7. (a)–(c) The term $\tilde{Q}'_{SH}$ and each term of its decomposition [Eqs. (9) and (11)] and (d)–(f) $\tilde{Q}'_{LH}$ and each term of its decomposition [Eqs. (10) and (12)] bin averaged as functions of the local wind direction θ at each grid point, with a bin width of 9°, 2010–22. Shading indicates the 95% confidence interval of the means in each bin, estimated using the Student's t distribution. The wind direction is expressed in the meteorological convention such that $\theta = 0°$ is the northerly wind; $\theta = 90°$ is the westerly wind; $\theta = 180°$ is the southerly wind; and $\theta = 270°$ is the easterly wind.

c. *Diagnosing the drivers of surface radiative heat flux variability*

In this section, we describe the relative importance of the Q'_{RAD} terms and diagnose the role of atmospheric variability in driving them in May–August, when Q'_{RAD} accounts for the majority of the variability in Q'_{net} (Fig. 4).

1) Downwelling shortwave anomalies dominate Q'_{RAD} variability

Downward shortwave radiative flux anomalies $Q'_{SW\downarrow}$ dominate variability in the May–August Q'_{RAD}, describing an average of 66% of the total variance (Fig. 10a), with a maximum value of 80% over the northern shelf and a value of 60% over most of the southern Bering Sea. Upward shortwave radiative flux anomalies $Q'_{SW\uparrow}$ and downward longwave radiative flux anomalies $Q'_{LW\downarrow}$ each account for an average of 17% of Q'_{RAD} variance (Figs. 10b,c). The maximum variance described by $Q'_{SW\uparrow}$ is 25% in the southeast, and the minimum is <5% over the northern shelf. The maximum variance described by $Q'_{LW\downarrow}$ is 25% in the western basin and along the climatological ice edge, with a minimum of 15% over the majority of the Bering Sea. Upward longwave radiative flux anomalies $Q'_{LW\uparrow}$ describe <1% of the variance in Q'_{RAD} (Fig. 10d). Because $Q_{LW\uparrow}$ is a function only of T_s, this indicates that ocean skin temperature anomalies are not significant drivers of the summertime surface radiative flux anomalies.

We evaluated the role of the CS and CRF radiative fluxes in driving the net shortwave radiative flux anomaly Q'_{SW} and net longwave radiative flux anomaly Q'_{LW} and found that CRF $Q'_{SW\downarrow}$ accounts for 77% of the variance of Q'_{SW} and CRF $Q'_{LW\downarrow}$ accounts for 67% of the variance of Q'_{LW} (assessed using DA techniques; not shown). The CS $Q'_{LW\downarrow}$ accounts for 26% of the variance of Q'_{LW}. The remaining terms, CRF

Brought to you by OREGON STATE UNIVERSITY | Unauthenticated | Downloaded 07/15/25 06:23 PM UTC

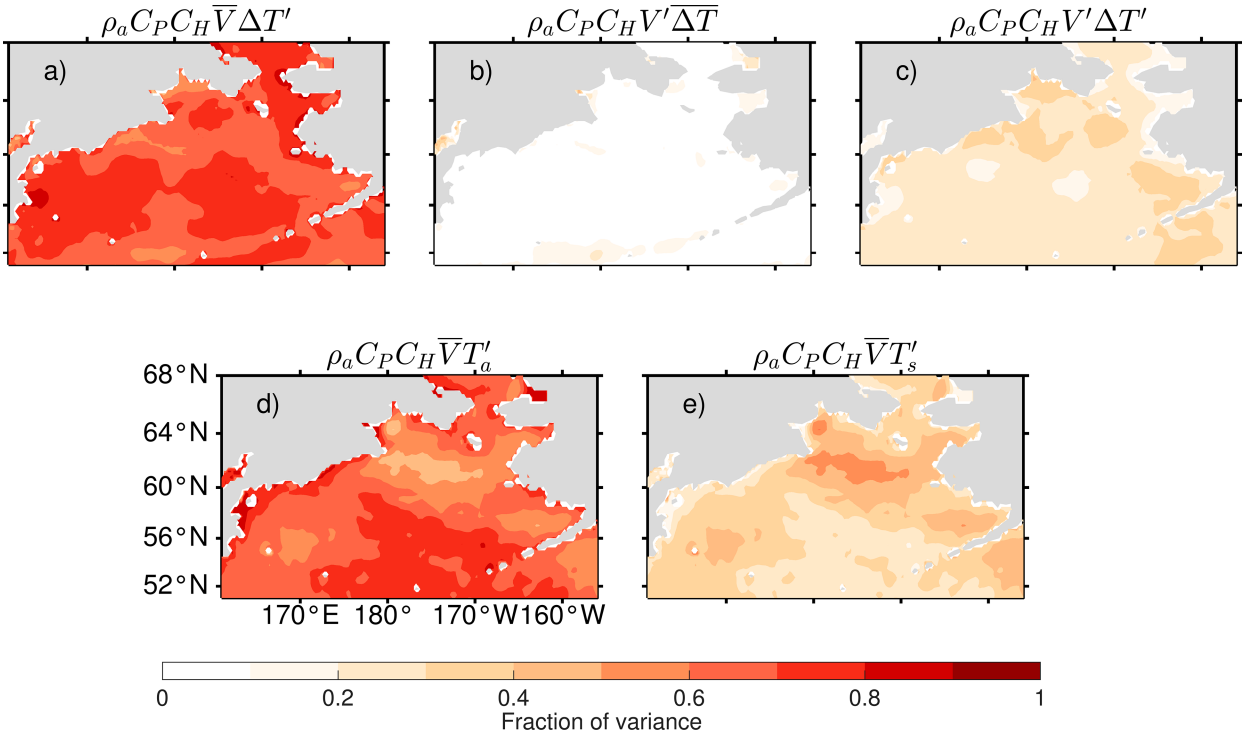

FIG. 8. (a)–(c) Fraction of the variance of the May–August daily ERA5 sensible heat flux anomaly decomposition $\tilde{Q}'_{\mathrm{SH}}$ accounted for by each term in its decomposition [Eq. (9)], computed using DA techniques. (d),(e) Fraction of the variance of term 1 in $\tilde{Q}'_{\mathrm{LH}}$ accounted for by the term proportional to T'_a and that proportional to T'_s [Eq. (9)].

$Q'_{\mathrm{SW}\uparrow}$, CS $Q'_{\mathrm{SW}\downarrow}$, and CS $Q'_{\mathrm{SW}\uparrow}$ for Q'_{SW} and CRF $Q'_{\mathrm{LW}\uparrow}$ and CS $Q'_{\mathrm{LW}\uparrow}$ forQ'_{LW}, account for less than 10% of the variance of their respective fields. At high latitudes, including the Bering Sea, clouds tend to be low in the atmosphere (Allan 2011; Forster et al. 2021), reflecting incoming surface radiation and trapping longwave radiation emitted by the surface (Shupe and Intrieri 2004; Forster et al. 2021). Because of the importance of clouds in the Bering Sea surface energy budget, and the dominance of the CRF radiative flux anomalies, in the following section, we assess the role of cloud coverage at different heights in the atmosphere in driving the summertime radiative flux anomalies.

2) Cloud variability and radiative flux anomalies

Cloud coverage at low, medium, and high levels in the atmosphere in ERA5 is defined as an aggregate over a range of σ-coordinate values. For a surface pressure of 1000 hPa, low cloud coverage (LCC) encompasses clouds occurring between the surface and 800 hPa; medium cloud coverage (MCC) encompasses clouds occurring between 800 and 450 hPa; and high cloud coverage (HCC) encompasses clouds on levels with a pressure less than 450 hPa. We developed an empirical linear regression model to describe the relationship between the anomalous CRF terms, and low cloud coverage anomalies LCC′, medium cloud coverage anomalies MCC′, and high cloud coverage anomalies HCC′:

$$Q'_{\mathrm{RAD}_{\mathrm{CRF}}} = \beta_1 \mathrm{LCC}' + \beta_2 \mathrm{MCC}' + \beta_3 \mathrm{HCC}'. \tag{13}$$

The magnitude of the resultant regression coefficients for each term β_i describes the effect of changes in the fractional cloud coverage at that level on the CRF surface radiative flux anomalies. The total cloud radiative forcing for both Q'_{RAD} and Q'_{SW} is negative at all cloud levels (Figs. 11a–f), meaning that clouds at all levels cool the surface by reflecting downwelling shortwave radiation upward. For the Q'_{RAD} model, the regression coefficient for the LCC′ is largest in magnitude in the southern Bering Sea, while the regression coefficient for the MCC′ is of a similar magnitude in the central Bering Sea and of a larger magnitude in the northern Bering Sea. The regression coefficient for the Q'_{SW} model and LCC′ is the largest of the three and is negative throughout the Bering Sea. The regression coefficient with MCC′ is also negative but is about a third of the magnitude smaller than that of LCC′. The regression coefficient for HCC′ is generally slightly negative for both the Q'_{RAD} and Q'_{SW} models but is not statistically different than zero for much of the Bering Sea. Therefore, LCC′ reflects the most incoming solar radiation relative to the other cloud coverage levels, with an effect that is most pronounced in the southern Bering Sea. For the CRF Q'_{LW} model, the regression coefficients at all levels are positive (Figs. 11g–i), indicating that longwave CRF warms the surface by absorbing and reemitting Q_{LW} toward the surface. The largest magnitude regression coefficient

Brought to you by OREGON STATE UNIVERSITY | Unauthenticated | Downloaded 07/15/25 06:23 PM UTC

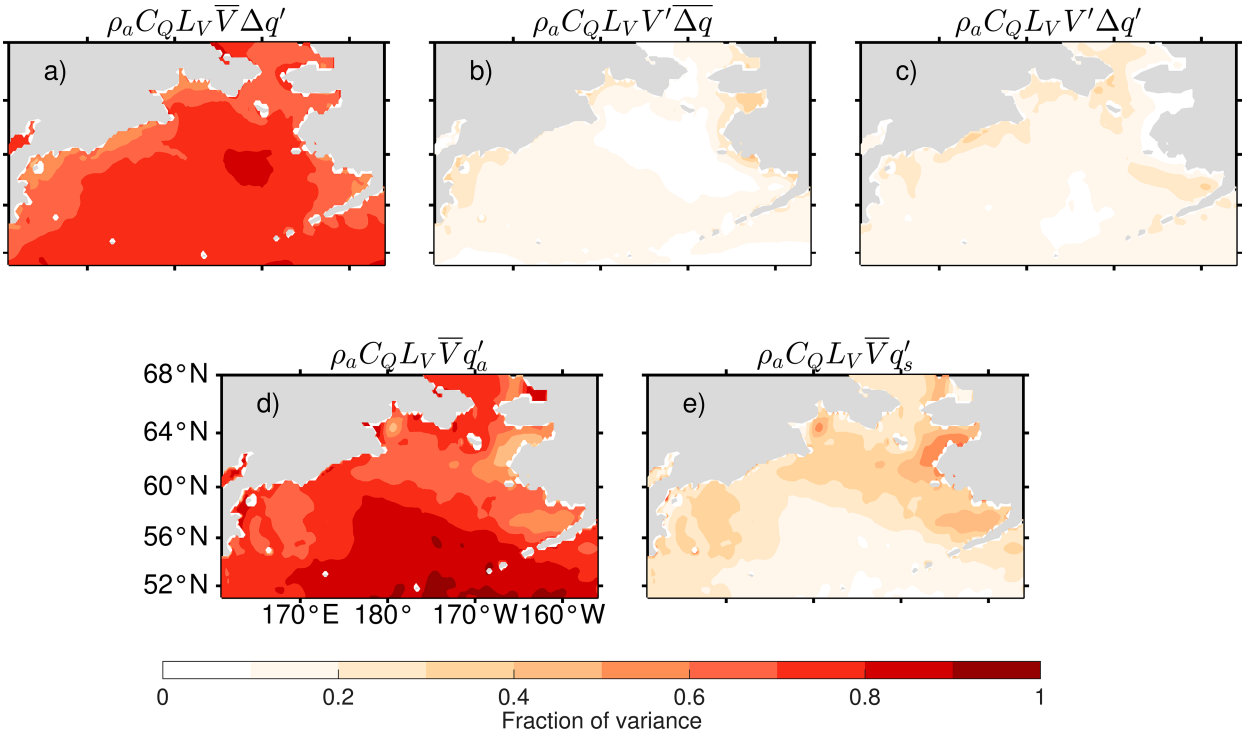

FIG. 9. (a)–(c) Fraction of the variance of the May–August daily ERA5 latent heat flux anomaly decomposition $\tilde{Q}'_{\mathrm{LH}}$ accounted for by each term in its decomposition [Eq. (10)], computed using DA techniques. (d),(e) Fraction of the variance of term 1 in $\tilde{Q}'_{\mathrm{LH}}$ accounted for by the term proportional to q'_a and that proportional to q'_s [Eq. (10)].

occurs for LCC′, and it is approximately half the size of the coefficient for Q'_{RAD} and Q'_{SW} at the same level. The coefficient for MCC′ is small throughout the Bering Sea, and the HCC′ coefficient is not statistically different than zero in most of the Bering Sea.

3) The radiative flux response to sea ice extent anomalies

Most of the variability in Q'_{SW}, which dominates variability in Q'_{RAD} in the summer months (>80%), is a result of the CRF Q'_{SW} (77%). However, during the month of May, there is a strong contribution to Q'_{RAD} (Fig. 12a) from anomalies in the CS Q'_{SW} (Fig. 12b), with more than 30% of the Q'_{RAD} variability in May in the northern Bering Sea due to CS Q'_{SW}. The CS Q_{SW} anomalies are dominated by the reflected CS shortwave flux (Fig. 12d). The signal is concentrated in the northern Bering Sea, in a region that would typically be ice covered in May (gray curve in Fig. 12), and is therefore a result of anomalously open ocean allowing for increased absorption of incoming shortwave radiation. The northern Bering Sea is ice free in at least some years of our analysis, resulting in an anomalous positive heat flux into the ocean that is a result of the decrease in surface albedo and the resultant decrease in the reflected shortwave radiative flux.

Although sea ice extent in the Bering Sea has not displayed a significant trend over recent decades (Parkinson and Cavalieri 2008; Cavalieri and Parkinson 2012), its interannual variability has increased (Danielson et al. 2011a), and the timing of sea ice advance has grown increasingly variable (Stabeno et al. 2007). Because the CS Q'_{SW} is concentrated in an area that is abnormally ice free, and because of the increase in sea ice extent variability and timing over recent decades, we evaluated the relationship between the CS Q'_{SW} and anomalies in the open ocean area (Fig. 13). We define the open ocean area anomalies as the difference between the total area of the Bering Sea that is ice free (according to the 15% sea ice criterion) for each day (2010–22) and the daily climatological average (1979–2010) total area of the Bering Sea that is ice free, presented as a fraction of the total Bering Sea area (Fig. 1a). The CS Q'_{SW} is positively correlated with anomalies in the open ocean area in February–March ($\rho^2 = 0.69 \pm 0.03$), with the largest magnitude flux anomalies and highest correlation observed in April and May ($\rho^2 = 0.82 \pm 0.02$). Sea ice extent in the Bering Sea tends to reach its maximum extent in February or March, before beginning its northward retreat in April, with the Bering Sea typically ice free by May or June (Danielson et al. 2011a; Baker et al. 2020). The large-magnitude CS Q'_{SW} in April and May occurs when there is an intersection between large changes in day length, solar zenith angle, and sea ice loss (Danielson et al. 2011b), which allows for large amounts of sunlight to be absorbed at the surface of the Bering Sea. There are years with large increases in the open ocean area in December and January, but the magnitude of the anomalous CS net shortwave flux anomalies into the ocean is generally small because of the lack of solar radiation in winter.

Brought to you by OREGON STATE UNIVERSITY | Unauthenticated | Downloaded 07/15/25 06:23 PM UTC

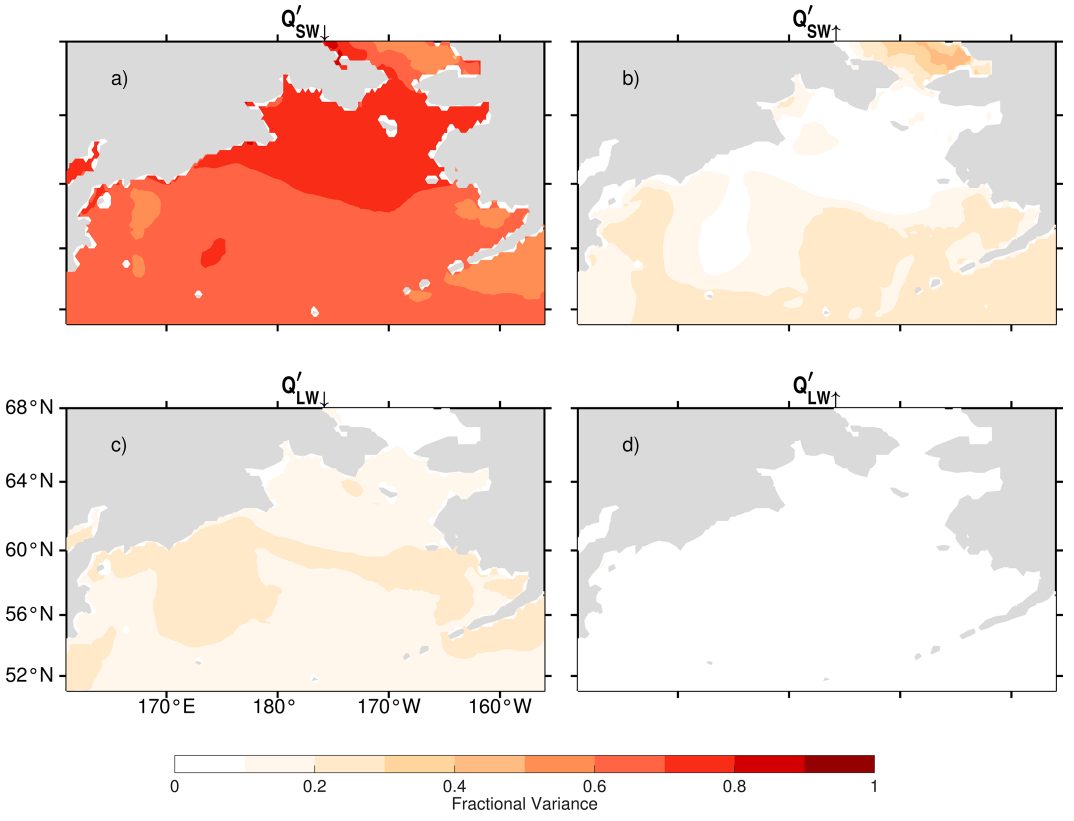

FIG. 10. (a)–(d) Fraction of the variance of the May–August daily ERA5 radiative heat flux anomaly Q'_{RAD}, 2010–22, described by the surface radiative flux terms on the right-hand side of Eq. (2), computed using DA techniques.

4) SUMMERTIME LOWER-TROPOSPHERIC TEMPERATURE VARIABILITY AND INCREASED THERMAL RADIATION

To assess the drivers of the CS $Q_{LW\downarrow}$ anomalies that account for 26% of the variance of $Q'_{LW\downarrow}$ in May–August, we analyze geopotential thickness anomalies in the lower troposphere between 1000 and 850 hPa. Geopotential thickness is directly proportional to the atmospheric layer average virtual air temperature, which is primarily a function of the layer average air temperature (Elliott et al. 1994). To determine whether anomalies in lower-tropospheric virtual temperature are driving CS $Q'_{LW\downarrow}$, we regressed geopotential thickness anomalies between 1000 and 850 hPa against the May–August CRF and CS $Q'_{LW\downarrow}$. The regression coefficient between the thickness anomalies and the CS $Q'_{LW\downarrow}$ is larger in magnitude (Fig. 14b) than that of the CRF $Q'_{LW\downarrow}$ (Fig. 14a), with a 1 W m^{-2} or larger increase in CS $Q'_{LW\downarrow}$ for a 1-m increase in geopotential thickness over much of the Bering Sea. Further analysis is necessary to determine the relative contribution of temperature and water vapor anomalies to the geopotential thickness variability and to then quantify their role in driving the observed CS $Q'_{LW\downarrow}$. In other parts of the Arctic, $Q'_{LW\downarrow}$ has been found to be significantly more sensitive to temperature variability than water vapor changes (Sedlar and Devasthale 2012), as the effect of specific humidity changes on geopotential thickness variability is relatively minor, especially at high latitudes (Elliott et al. 1994).

d. *Estimating the effect of surface heat flux variability on the Bering Sea temperature*

Because the ocean can be understood as an integrator of atmospheric white noise forcing (Frankignoul and Hasselmann 1977; Di Lorenzo et al. 2010), we estimated the effect of the surface heat flux anomalies on the ocean state by computing an annual cumulative potential mixed-layer heating term for each Q'_{net} term. We defined the annual cumulative potential heating terms as the time integral of each F' component [Eq. (7)] from October–September (Fig. 15). This period was chosen because October marks the typical beginning of the sea ice season (Overland 1981) and the winter storm season (Pickart et al. 2009), thus capturing a "climatological" year in the Bering Sea and providing insight into the interannually varying potential effect of surface heat flux anomalies on the ocean state. In seven of the 12 years considered, the net cumulative potential heating term is positive (black squares in Fig. 15). The largest magnitude cumulative potential heating occurred in 2013/14 (1.83°C) and 2017/18 (1.28°C). In 2013/14, Q'_{THF} (1.06°C) accounts for most of the net cumulative heating, while in 2017/18, Q'_{SW} (0.68°C) and Q'_{LW} (0.66°C) contribute a similar amount. In every year considered, the cumulative potential heating from $Q'_{LW\uparrow}$ and $Q'_{LW\downarrow}$ is of opposite sign, and in all years except 2011/12, the cumulative potential heating due to $Q'_{LW\uparrow}$ is negative, while that due to $Q'_{LW\downarrow}$ is positive. The tendency for $Q'_{LW\uparrow}$ to be negative is

Brought to you by OREGON STATE UNIVERSITY | Unauthenticated | Downloaded 07/15/25 06:23 PM UTC

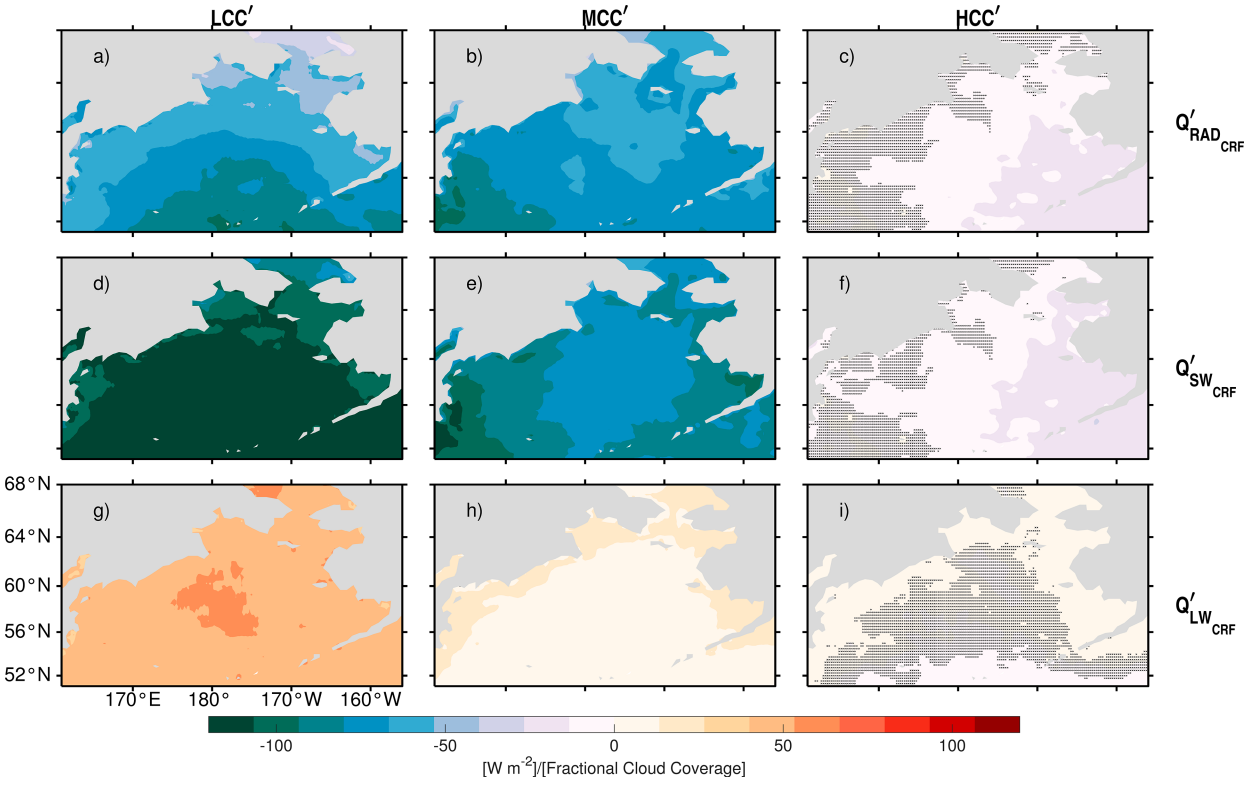

FIG. 11. Linear regression coefficients from an empirical linear regression model relating the relative contribution of (top) low, (middle) medium, and (bottom) high cloud anomalies to the (a)–(c) Q'_{RAD} CRF variability, (d)–(f) Q'_{SW} CRF variability, and (g)–(i) Q'_{LW} CRF variability. Regression coefficient values that are not statistically different than zero (at the 95% confidence level) are noted by black shading. The cloud amounts are given in terms of a fraction of a grid cell, so the units of the regression coefficients are watts per square meter per fractional change.

likely a result of anomalously elevated surface ocean temperatures, while positive downward longwave radiative flux anomalies $Q'_{LW\downarrow}$ are likely a result of either an anomalously warm atmosphere driving increased thermal radiation into the ocean or increased $Q'_{LW\uparrow}$ out of the ocean that is absorbed and reemitted downward in the lower troposphere.

We additionally estimated the annual (October–September) change in ocean surface temperature over the same period using ERA5 fields of SSTA, which we have denoted as ΔSST (white diamonds in Fig. 15), to evaluate whether variability in the surface heat exchange has a similar influence on SSTA as it potentially does for MLTa. If ΔSST and the net cumulative potential heating rate are similar in a given year, it suggests that upper-ocean temperature anomalies in the Bering Sea in that year are primarily a function of anomalies in the surface heat flux. In most years, the change in SSTA and the net cumulative potential heating term are of a similar sign and magnitude. The annual change in SSTA and the net cumulative heating potential rate differed by more 0.5°C for four of the years considered: 2014/15, 2016/17, 2018/19, and 2021/22. MHWs were observed in three of these years, with designated MHWs in the eastern Bering Sea shelf region in 2014/15 and 2018/19 (Belkin and Short 2023; Szuwalski et al. 2023) and an MHW present in the Aleutian basin beginning in summer 2021 (Barkhordarian et al. 2022). Further discussion about the difference between the annual change in SSTA and the net cumulative heating is discussed in the following section.

4. Discussion and conclusions

This study investigated the seasonally varying processes responsible for anomalies in the Bering Sea air–sea heat exchange over 2010–22. The primary result is that the atmosphere plays a dominant role in driving surface heat flux anomalies throughout the year. Anomalies in the surface turbulent heat fluxes account for most of the net surface heat flux variability in September–April and are primarily a consequence of near-surface air temperature and humidity anomalies. The sign and magnitude of the turbulent heat flux anomalies and the airmass anomalies that drive them are cyclic functions of wind direction, indicative of the importance of large-scale atmospheric circulation in the turbulent heat flux variability. These results clarify the role of the near-surface wind on Q'_{THF}, showing that wind direction is more important than anomalies in the wind speed in driving the surface turbulent heat flux variability. In the remaining months of the year (May–August), anomalies in the downward shortwave radiation dominate net surface heat flux variability and are primarily a function of variability in cloud coverage. The

Brought to you by OREGON STATE UNIVERSITY | Unauthenticated | Downloaded 07/15/25 06:23 PM UTC

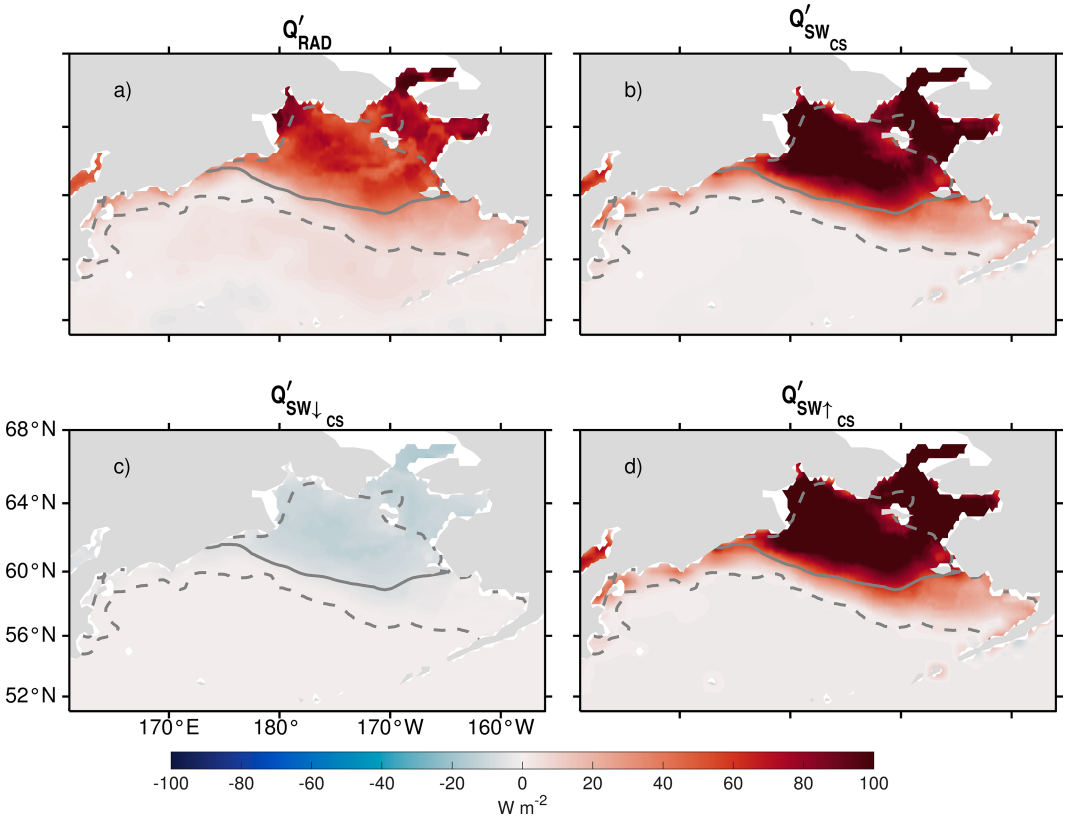

FIG. 12. Mean value of the May 2010–22 (a) Q'_{RAD}, (b) $Q'_{\mathrm{SW_{CS}}}$, (c) $Q'_{\mathrm{SW\downarrow_{CS}}}$, and (d) $Q'_{\mathrm{SW\uparrow_{CS}}}$. The climatological average (1979–2010) sea ice edge for May is depicted by the solid gray contours, with the minimum (2017) and maximum (2012) May sea ice extent over the period of interest (2010–22) depicted by the dashed gray contours.

second largest term contributing to Q'_{net} in these months is $Q'_{\mathrm{LW\downarrow}}$, which is largely a result of geopotential thickness anomalies in the lower troposphere. Furthermore, in May, there is a contribution to Q'_{SW} from the clear-sky net shortwave radiation that is a result of anomalously low sea ice extent in the Bering Sea that coincides with increasing day length/solar zenith angle, which together result in a decrease in reflected incoming shortwave radiation at the surface. We evaluated the drivers of Q'_{THF} in May–August and found that, although they were still primarily driven by atmospheric variability, there was an increased contribution from T'_s and q'_s, in comparison with September–April. This is suggestive of an increase in the importance of ocean variability in altering the air–sea heat exchange in the summer.

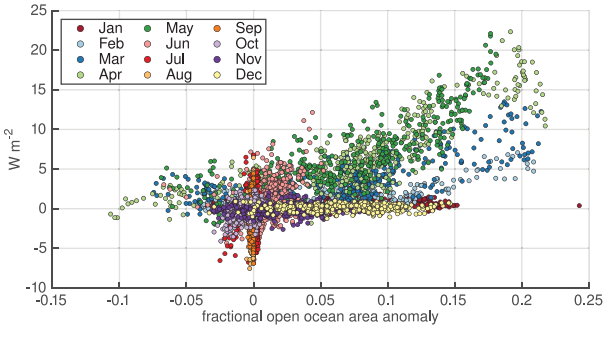

FIG. 13. Scatterplot of the fractional open ocean area anomaly (x axis) and the CS net shortwave radiative flux anomalies (y axis). The fractional open ocean area anomalies are computed as the difference between the area of the Bering Sea that is considered ice free for our analysis (≤15%) and the climatological ice-free area, as a fraction of the total area of the Bering Sea, color coded by month of the year, 2010–22.

We also estimated the potential ocean MLT response to the atmospherically driven surface heat flux anomalies and found that the estimate was of a similar order as the change in temperature estimated using SST fields during most years. During years in which the observed change in SST differed drastically from our estimated potential change (i.e., 2014/15, 2016/17, 2018/19, and 2021/22), other ocean dynamical processes are likely important. For example, vertical diffusion, a key process in the Bering Sea upper-ocean temperature variability (Hayden and O'Neill 2024), may play an important role by transporting heat below the mixed-layer. This heat may be stored beneath the mixed layer before reemerging at the surface (Alexander et al. 1999). Northward oceanic heat flux through the Bering Strait has increased in recent years (2014–18), largely due to increased advection from the Bering Sea shelf, as well as increased air–sea heat fluxes into the

Brought to you by OREGON STATE UNIVERSITY | Unauthenticated | Downloaded 07/15/25 06:23 PM UTC

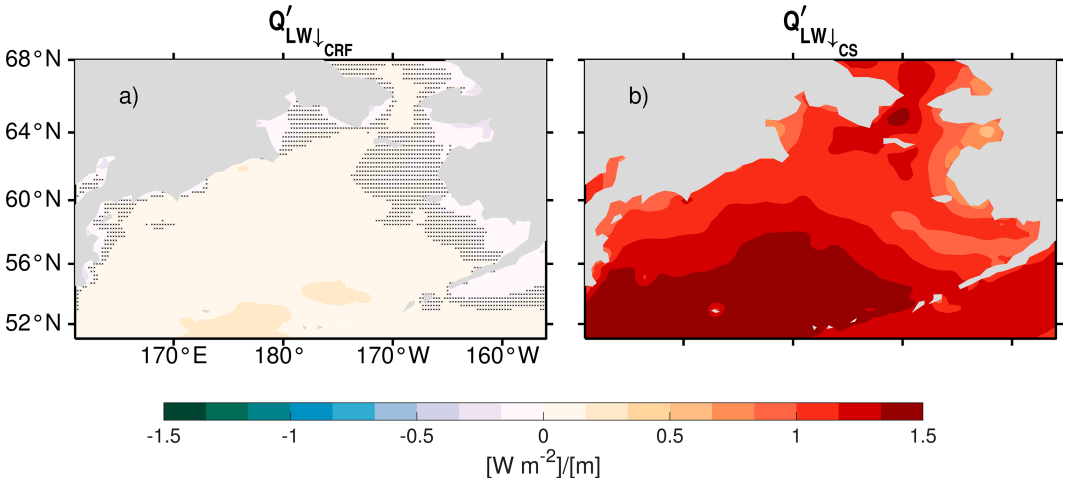

FIG. 14. Regression coefficients between anomalies in the geopotential thickness between 1000 and 850 hPa and the (a) cloudy sky $\tilde{Q}'_{LW\downarrow}$ and (b) CS $\tilde{Q}'_{LW\downarrow}$. Grid cells for which the regression coefficient is not statistically significant at the 95% confidence interval are shaded in black.

shelf region (Danielson et al. 2020). The increase in heat fluxed northward from the Bering Sea due to amplified advection and anomalously warm ocean temperatures driven by surface heat flux anomalies describes a possible formation mechanism for the "heat bombs" responsible for accelerating Arctic sea ice loss (MacKinnon et al. 2021; Monroe 2021). Furthermore, MHWs were observed in the Bering Sea in 2014/15, in 2018/19, and in the summer of 2021 (Belkin and Short 2023; Szuwalski et al. 2023; Barkhordarian et al. 2022), which have been linked to advection of anomalously warm water from the North Pacific (Basyuk and Zuenko 2020; Belkin and Short 2023). Finally, to first order, the equivalent heating terms were relatively insensitive to the use of a climatological MLD, but some of the difference between the estimated potential change due to anomalies in the net surface flux and ΔSST could be addressed by using daily MLD fields, which are not yet available for our full period of analysis through ECCO.

In this analysis, we masked sea ice, which allowed us to focus only on air–sea interactions. In general, sea ice coverage reduces the exchange of heat between the ocean and the atmosphere by reflecting the small amount of wintertime shortwave radiation incident at the surface, by insulating the upper ocean from cold sub-Arctic air, and by damping surface waves which tend to enhance turbulent exchanges in the upper ocean. Therefore, we expect that our decision to mask sea ice will tend to remove grid cells with small heat fluxes and will have a small basin-scale impact on ocean surface temperature anomalies and our results. We estimated the effect of the sea ice masking by comparing the net cumulative heating resulting

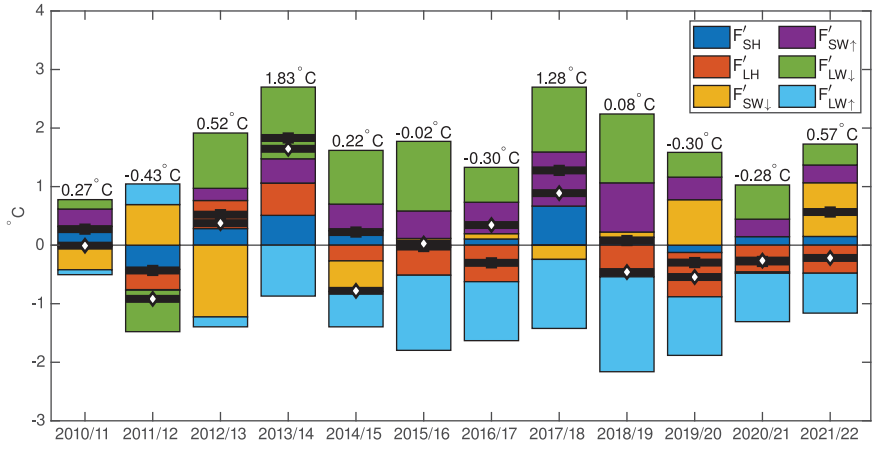

FIG. 15. Annual (October–September) cumulative potential heating in degrees Celsius due to anomalies in each term in Eq. (2). The net cumulative potential heating due to the contribution of all six terms combined is denoted by the black square in each bar chart, and its value is noted above each bar. The estimated ERA5 ΔSST_a over the October–September climatological year is denoted by the white diamonds.

Brought to you by OREGON STATE UNIVERSITY | Unauthenticated | Downloaded 07/15/25 06:23 PM UTC

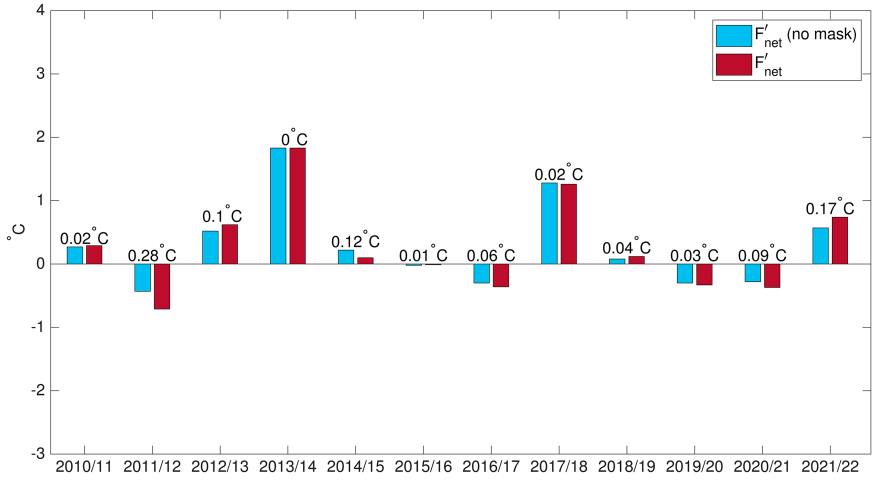

FIG. 16. Annual (October–September) net cumulative potential heating in degrees Celsius due to Q'_{net}. Blue bars are computed from ice-masked fields and are equivalent to Fig. 15, while the red bars are computed from the unmasked fields. The magnitude of the difference between the masked and unmasked fields is shown above each bar.

from the sea ice masked and unmasked fields (Fig. 16) and found that removing sea ice generally had a small effect on the basin-scale results. 2010/11 and 2021/22 were exceptions to this, and these were also years in which Bering Sea sea ice concentration was higher than average, extending further south in comparison with the climatological (1981–2010) average (Stabeno and Bell 2019; National Snow and Ice Data Center 2022). We hypothesize that the anomalously high sea ice concentration in 2011/12 insulated the Bering Sea, resulting in reduced upper-ocean heat loss in comparison with our ice-masked analysis. In 2021/22, the cumulative heating was positive and larger for the unmasked fields, which does not align with our hypothesis about sea ice insulation, suggesting the need for further analysis.

The results described in this work and in a previous manuscript (Hayden and O'Neill 2024) indicate that the atmosphere is a key driver of upper-ocean thermal variability in the Bering Sea. Recent studies have described changes in the large-scale atmospheric circulation over the North Pacific that may be contributing to the observed increase in surface heat flux variability. The North Pacific storm track has shifted poleward over recent decades (Rudeva and Simmonds 2015; Wang et al. 2017), increased variability in the jet stream and associated persistent weather patterns have been described (Francis and Vavrus 2015), and positive trends in blocking frequency over the Bering Sea have been identified (Woollings et al. 2018). These large-scale shifts in North Pacific atmospheric circulation may be relevant to the observed seasonal variability of the turbulent heat fluxes in the Bering Sea. Furthermore, large-scale modes of North Pacific climate variability may contribute to the atmospheric variability that we have identified as key to Bering Sea temperature anomalies, as low-frequency interdecadal-to-decadal climate oscillations play an important role in the Bering Sea climate variability (i.e., Wooster and Hollowed 1995; Overland et al. 2012; Yang et al. 2020). Further analysis is necessary to quantify the contribution of atmospheric variability to the observed surface heat flux anomalies across a range of time and space scales, from synoptic-scale weather variability to relatively slower modes of variability, including intraseasonal, annual, and interannual bands.

Acknowledgments. E.E.H. is supported by the National Defense Science and Engineering (NDSEG) Fellowship. L.W.O. is funded in part with funding from the Jet Propulsion Laboratory, California Institute of Technology (Contract 1612966), under a grant awarded by the NASA MEASURES program (NNH17ZDA001N-MEASURES); NASA Grant 80NSSC19K1117 as part of the NASA Physical Oceanography Program; and NASA Grant 80NSSC21K1188 as part of the NASA Ocean Surface Topography Science Team. S.F.Z. is funded by NASA's SASSIE program 80NSSC21K0832; NSF Awards 2023020, 2316818, and 2241792; ONR Award N00014-22-1-2405; and DOE's WFIP3 Program DEEE0009424. Maps in this paper were generated using the M_Map Matlab Package (Pawlowicz 2020), with perceptually uniform color maps from the cmocean package (Thyng et al. 2016).

Data availability statement. All ERA5 data are publicly available through the Copernicus Climate Change Climate Data Store (https://cds.climate.copernicus.eu). All ECCO V4r4 data are publicly available at https://ecco.jpl.nasa.gov/. The monthly PDO index is available through NOAA NCEI (https://www.ncei.noaa.gov/pub/data/cmb/ersst/v5/index/ersst.v5.pdo.dat).

APPENDIX

Turbulent Heat Flux Decomposition

We derived our decomposition of Q'_{SH} and Q'_{LH} using a bulk formula for the sensible and latent heat flux and Reynolds averaging. A detailed derivation of $\tilde{Q}'_{SH}$ is shown here, with

Brought to you by OREGON STATE UNIVERSITY | Unauthenticated | Downloaded 07/15/25 06:23 PM UTC

a similar derivation and result for $\tilde{Q}'_{\mathrm{LH}}$. Reynolds averaging is defined by $X = \overline{X} + X'$ (or $X' = X - \overline{X}$), where baseline climatological means are denoted by an overbar and anomalies from the mean relative to the baseline (1979–2010) climatology are denoted by a prime. Beginning with a bulk formula for Q_{SH}:

$$\begin{aligned}
\frac{Q_{\mathrm{SH}}}{\rho_a C_P C_H} &= V\Delta T \\
&= (\overline{V} + V')(\overline{\Delta T} + \Delta T') \\
&= \overline{V}\,\overline{\Delta T} + \overline{V}\Delta T' + V'\overline{\Delta T} + V'\Delta T' \\
\frac{\overline{Q_{\mathrm{SH}}}}{\rho_a C_P C_H} &= \overline{\overline{V}\,\overline{\Delta T}} + \overline{\overline{V}\Delta T'} + \overline{V'\overline{\Delta T}} + \overline{V'\Delta T'} \\
&= \overline{V}\,\overline{\Delta T} + \overline{V'\Delta T'} \\
\left(\frac{Q_{\mathrm{SH}}}{\rho_a C_P C_H}\right)' &= \frac{Q_{\mathrm{SH}}}{\rho_a C_P C_H} - \frac{\overline{Q_{\mathrm{SH}}}}{\rho_a C_P C_H} \\
&= \rho_a C_P C_H(\overline{V}\Delta T' + V'\overline{\Delta T} + V'\Delta T' - \overline{V'\Delta T'}).
\end{aligned}$$

The last term on the right-hand side of the equation above is the mean contribution of the covarying V' and $\Delta T'$ terms, a negligible term that is neglected for the remainder of this analysis. The decomposed Q'_{SH} is composed of three terms:

$$\tilde{Q}'_{\mathrm{SH}} = \rho_a C_P C_H(\overline{V}\Delta T' + V'\overline{\Delta T} + V'\Delta T').$$

In a similar fashion, we derived a decomposition of Q'_{LH} as

$$\tilde{Q}'_{\mathrm{LH}} = \rho_a C_E L_v(\overline{V}\Delta q' + V'\overline{\Delta q} + V'\Delta q').$$

REFERENCES

Alexander, M. A., C. Deser, and M. S. Timlin, 1999: The reemergence of SST anomalies in the North Pacific Ocean. *J. Climate*, **12**, 2419–2433, https://doi.org/10.1175/1520-0442(1999)012<2419:TROSAI>2.0.CO;2.

Allan, R. P., 2011: Combining satellite data and models to estimate cloud radiative effect at the surface and in the atmosphere. *Meteor. Appl.*, **18**, 324–333, https://doi.org/10.1002/met.285.

Amaya, D. J., A. J. Miller, S.-P. Xie, and Y. Kosaka, 2020: Physical drivers of the summer 2019 North Pacific marine heatwave. *Nat. Commun.*, **11**, 1903, https://doi.org/10.1038/s41467-020-15820-w.

Azen, R., and D. V. Budescu, 2003: The dominance analysis approach for comparing predictors in multiple regression. *Psychol. Methods*, **8**, 129–148, https://doi.org/10.1037/1082-989X.8.2.129.

Baker, M. R., K. K. Kivva, M. N. Pisareva, J. T. Watson, and J. Selivanova, 2020: Shifts in the physical environment in the Pacific Arctic and implications for ecological timing and conditions. *Deep-Sea Res. II*, **177**, 104802, https://doi.org/10.1016/j.dsr2.2020.104802.

Barkhordarian, A., D. M. Nielsen, and J. Baehr, 2022: Recent marine heatwaves in the North Pacific warming pool can be attributed to rising atmospheric levels of greenhouse gases. *Commun. Earth Environ.*, **3**, 131, https://doi.org/10.1038/s43247-022-00461-2.

Basyuk, E., and Y. Zuenko, 2020: Extreme oceanographic conditions in the northwestern Bering Sea in 2017–2018. *Deep-Sea Res. II*, **181–182**, 104909, https://doi.org/10.1016/j.dsr2.2020.104909.

Belkin, I. M., and J. W. Short, 2023: Echoes of the 2013–2015 marine heat wave in the eastern Bering Sea and consequent biological responses. *J. Mar. Sci. Eng.*, **11**, 958, https://doi.org/10.3390/jmse11050958.

Bond, N. A., M. F. Cronin, H. Freeland, and N. Mantua, 2015: Causes and impacts of the 2014 warm anomaly in the NE Pacific. *Geophys. Res. Lett.*, **42**, 3414–3420, https://doi.org/10.1002/2015GL063306.

Bourassa, M. A., and Coauthors, 2013: High-latitude ocean and sea ice surface fluxes: Challenges for climate research. *Bull. Amer. Meteor. Soc.*, **94**, 403–423, https://doi.org/10.1175/BAMS-D-11-00244.1.

Budescu, D. V., 1993: Dominance analysis: A new approach to the problem of relative importance of predictors in multiple regression. *Psychol. Bull.*, **114**, 542–551, https://doi.org/10.1037/0033-2909.114.3.542.

Carvalho, K. S., T. E. Smith, and S. Wang, 2021: Bering Sea marine heatwaves: Patterns, trends and connections with the Arctic. *J. Hydrol.*, **600**, 126462, https://doi.org/10.1016/j.jhydrol.2021.126462.

Cavalieri, D. J., and C. L. Parkinson, 2012: Arctic sea ice variability and trends, 1979–2010. *Cryosphere*, **6**, 881–889, https://doi.org/10.5194/tc-6-881-2012.

Cayan, D. R., 1992a: Latent and sensible heat flux anomalies over the northern oceans: Driving the sea surface temperature. *J. Phys. Oceanogr.*, **22**, 859–881, https://doi.org/10.1175/1520-0485(1992)022<0859:LASHFA>2.0.CO;2.

——, 1992b: Variability of latent and sensible heat fluxes estimated using bulk formulae. *Atmos.–Ocean*, **30** (1), 1–42, https://doi.org/10.1080/07055900.1992.9649429.

Chen, H.-H., Y. Wang, P. Xiu, Y. Yu, W. Ma, and F. Chai, 2023: Combined oceanic and atmospheric forcing of the 2013/14 marine heatwave in the northeast Pacific. *npj Climate Atmos. Sci.*, **6**, 3, https://doi.org/10.1038/s41612-023-00327-0.

Cheung, W. W. L., and T. L. Frölicher, 2020: Marine heatwaves exacerbate climate change impacts for fisheries in the northeast Pacific. *Sci. Rep.*, **10**, 6678, https://doi.org/10.1038/s41598-020-63650-z.

Danielson, S., E. Curchitser, K. Hedstrom, T. Weingartner, and P. Stabeno, 2011a: On ocean and sea ice modes of variability in the Bering Sea. *J. Geophys. Res.*, **116**, C12034, https://doi.org/10.1029/2011JC007389.

——, L. Eisner, T. Weingartner, and K. Aagaard, 2011b: Thermal and haline variability over the central Bering Sea shelf: Seasonal and interannual perspectives. *Cont. Shelf Res.*, **31**, 539–554, https://doi.org/10.1016/j.csr.2010.12.010.

Danielson, S. L., and Coauthors, 2020: Manifestation and consequences of warming and altered heat fluxes over the Bering and Chukchi Sea continental shelves. *Deep-Sea Res. II*, **177**, 104781, https://doi.org/10.1016/j.dsr2.2020.104781.

Deser, C., and M. S. Timlin, 1997: Atmosphere–ocean interaction on weekly timescales in the North Atlantic and Pacific. *J. Climate*, **10**, 393–408, https://doi.org/10.1175/1520-0442(1997)010<0393:AOIOWT>2.0.CO;2.

Di Lorenzo, E., and N. Mantua, 2016: Multi-year persistence of the 2014/15 North Pacific marine heatwave. *Nat. Climate Change*, **6**, 1042–1047, https://doi.org/10.1038/nclimate3082.

Brought to you by OREGON STATE UNIVERSITY | Unauthenticated | Downloaded 07/15/25 06:23 PM UTC

——, K. M. Cobb, J. C. Furtado, N. Schneider, B. T. Anderson, A. Bracco, M. A. Alexander, and D. J. Vimont, 2010: Central Pacific El Niño and decadal climate change in the North Pacific Ocean. *Nat. Geosci.*, **3**, 762–765, https://doi.org/10.1038/ngeo984.

ECCO Consortium, I. Fukumori, O. Wang, I. Fenty, G. Forget, P. Heimbach, and R. M. Ponte, 2021: Synopsis of the ECCO Central production global ocean and sea-ice state estimate, version 4 release 4. Zenodo, accessed 15 March 2021, https://doi.org/10.5281/zenodo.4533349.

ECMWF, 2019: European State of the Climate 2019—Headline climate indicators: Sea ice. Accessed 10 July 2023, https://climate.copernicus.eu/ESOTC/2019/sea-ice.

Elliott, W. P., D. J. Gaffen, J. K. Angell, and J. D. W. Kahl, 1994: The effect of moisture on layer thicknesses used to monitor global temperatures. *J. Climate*, **7**, 304–308, https://doi.org/10.1175/1520-0442(1994)007<0304:TEOMOL>2.0.CO;2.

Feng, C., X. Zhang, J. Xu, S. Yang, S. Guan, K. Jia, and Y. Yao, 2023: Comprehensive assessment of global atmospheric downward longwave radiation in the state-of-the-art reanalysis using satellite and flux tower observations. *Climate Dyn.*, **60**, 1495–1521, https://doi.org/10.1007/s00382-022-06366-2.

Forget, G., J.-M. Campin, P. Heimbach, C. N. Hill, R. M. Ponte, and C. Wunsch, 2015: ECCO version 4: An integrated framework for non-linear inverse modeling and global ocean state estimation. *Geosci. Model Dev.*, **8**, 3071–3104, https://doi.org/10.5194/gmd-8-3071-2015.

Forster, P., and Coauthors, 2021: The Earth's energy budget, climate feedbacks and climate sensitivity. *Climate Change 2021—The Physical Science Basis*, V. Masson-Delmotte et al., Eds., Cambridge University Press, 923–1054, https://doi.org/10.1017/9781009157896.009.

Francis, J. A., and S. J. Vavrus, 2015: Evidence for a wavier jet stream in response to rapid Arctic warming. *Environ. Res. Lett.*, **10**, 014005, https://doi.org/10.1088/1748-9326/10/1/014005.

Frankignoul, C., 1985: Sea surface temperature anomalies, planetary waves, and air-sea feedback in the middle latitudes. *Rev. Geophys.*, **23**, 357–390, https://doi.org/10.1029/RG023i004p00357.

——, and K. Hasselmann, 1977: Stochastic climate models, Part II Application to sea-surface temperature anomalies and thermocline variability. *Tellus*, **29A**, 289–305, https://doi.org/10.3402/tellusa.v29i4.11362.

Frölicher, T. L., E. M. Fischer, and N. Gruber, 2018: Marine heatwaves under global warming. *Nature*, **560**, 360–364, https://doi.org/10.1038/s41586-018-0383-9.

Fukumori, I., O. Wang, I. Fenty, G. Forget, P. Heimbach, and R. Ponte, 2017: ECCO Central estimate (version 4 release 4). https://ecco.jpl.nasa.gov/.

Graham, R. M., S. R. Hudson, and M. Maturilli, 2019: Improved performance of ERA5 in Arctic gateway relative to four global atmospheric reanalyses. *Geophys. Res. Lett.*, **46**, 6138–6147, https://doi.org/10.1029/2019GL082781.

Halkides, D. J., D. E. Waliser, T. Lee, D. Menemenlis, and B. Guan, 2015: Quantifying the processes controlling intraseasonal mixed-layer temperature variability in the tropical Indian Ocean. *J. Geophys. Res. Oceans*, **120**, 692–715, https://doi.org/10.1002/2014JC010139.

Hayden, E. E., and L. W. O'Neill, 2024: Processes contributing to Bering Sea temperature variability in the late twentieth and early twenty-first century. *J. Climate*, **37**, 41–58, https://doi.org/10.1175/JCLI-D-23-0331.1.

Hersbach, H., and Coauthors, 2020: The ERA5 global reanalysis. *Quart. J. Roy. Meteor. Soc.*, **146**, 1999–2049, https://doi.org/10.1002/qj.3803.

Hobday, A. J., and Coauthors, 2016: A hierarchical approach to defining marine heatwaves. *Prog. Oceanogr.*, **141**, 227–238, https://doi.org/10.1016/j.pocean.2015.12.014.

IFS Documentation–Part II, 2023: IFS Documentation CY48R1 - Part II: Data assimilation. ECMWF Doc., 108 pp., https://doi.org/10.21957/a744f32e74.

IFS Documentation–Part IV, 2023: IFS Documentation CY38R1 - Part IV: Physical processes. ECMWF Doc., 266 pp., https://doi.org/10.21957/02054f0fbf.

Kong, B., N. Liu, L. Lin, Y. He, Y. Wang, and Z. Pan, 2019: Assessment of meteorological variables and heat fluxes from atmospheric reanalysis and objective analysis products over the Bering Sea. *Int. J. Climatol.*, **39**, 4429–4450, https://doi.org/10.1002/joc.6083.

MacKinnon, J. A., and Coauthors, 2021: A warm jet in a cold ocean. *Nat. Commun.*, **12**, 2418, https://doi.org/10.1038/s41467-021-22505-5.

Matthews, J. L., G. Peng, W. N. Meier, and O. Brown, 2020: Sensitivity of Arctic sea ice extent to sea ice concentration threshold choice and its implication to ice coverage decadal trends and statistical projections. *Remote Sens.*, **12**, 807, https://doi.org/10.3390/rs12050807.

Meier, W. N., and Coauthors, 2021: Arctic Report Card 2021: Sea ice. NOAA Tech. Rep. OAR ARC 21-05, 9 pp., https://doi.org/10.25923/y2wd-fn85..

Monroe, R., 2021: The "heat bombs" destroying Arctic sea ice. UC San Diego, https://scripps.ucsd.edu/news/heat-bombs-destroying-arctic-sea-ice.

National Snow and Ice Data Center, 2022: Arctic sea ice this January: So last decade. Accessed 24 May 2024, https://nsidc.org/sea-ice-today/analyses/arctic-sea-ice-january-so-last-decade.

Overland, J. E., 1981: Marine Climatology of the Bering Sea. *The Eastern Bering Sea Shelf: Oceanography and Resources*, D. W. Hood and J. A. Calder, Eds., U.S. Department of Commerce, National Oceanic and Atmospheric Administration, University of Washington Press, 15–22.

——, M. Wang, K. R. Wood, D. B. Percival, and N. A. Bond, 2012: Recent Bering Sea warm and cold events in a 95-year context. *Deep-Sea Res. II*, **65**, 6–13, https://doi.org/10.1016/j.dsr2.2012.02.013.

Parkinson, C. L., and D. J. Cavalieri, 2008: Arctic sea ice variability and trends, 1979–2006. *J. Geophys. Res.*, **113**, C07003, https://doi.org/10.1029/2007JC004558.

Pawlowicz, R., 2020: M_Map: A mapping package for MATLAB, version 1.4 m, (Computer software). The University of British Columbia, https://www-old.eoas.ubc.ca/~rich/map.html.

Phillips, B., and L. O'Neill, 2020: Observational analysis of extratropical cyclone interactions with northeast Pacific sea surface temperature anomalies. *J. Climate*, **33**, 6745–6763, https://doi.org/10.1175/JCLI-D-19-0853.1.

Piatt, J. F., and Coauthors, 2020: Extreme mortality and reproductive failure of common murres resulting from the northeast Pacific marine heatwave of 2014–2016. *PLOS ONE*, **15**, e0226087, https://doi.org/10.1371/journal.pone.0226087.

Pickart, R. S., A. M. Macdonald, G. W. K. Moore, I. A. Renfrew, J. E. Walsh, and W. S. Kessler, 2009: Seasonal evolution of Aleutian Low pressure systems: Implications for the North Pacific subpolar circulation. *J. Phys. Oceanogr.*, **39**, 1317–1339, https://doi.org/10.1175/2008JPO3891.1.

Brought to you by OREGON STATE UNIVERSITY | Unauthenticated | Downloaded 07/15/25 06:23 PM UTC

Ramanathan, V., R. D. Cess, E. F. Harrison, P. Minnis, B. R. Barkstrom, E. Ahmad, and D. Hartmann, 1989: Cloud-radiative forcing and climate: Results from the Earth Radiation Budget Experiment. *Science*, **243**, 57–63, https://doi.org/10.1126/science.243.4887.57.

Reed, R. K., 2003: A surface heat flux climatology over a region of the eastern Bering Sea. *Cont. Shelf Res.*, **23**, 1255–1263, https://doi.org/10.1016/S0278-4343(03)00128-6.

——, and P. J. Stabeno, 2002: Surface heat fluxes and subsurface heat content at a site over the southeastern Bering Sea shelf, May–July 1996. *Deep-Sea Res. II*, **49**, 5911–5917, https://doi.org/10.1016/S0967-0645(02)00325-9.

Renfrew, I. A., and Coauthors, 2021: An evaluation of surface meteorology and fluxes over the Iceland and Greenland Seas in ERA5 reanalysis: The impact of sea ice distribution. *Quart. J. Roy. Meteor. Soc.*, **147**, 691–712, https://doi.org/10.1002/qj.3941.

Rudeva, I., and I. Simmonds, 2015: Variability and trends of global atmospheric frontal activity and links with large-scale modes of variability. *J. Climate*, **28**, 3311–3330, https://doi.org/10.1175/JCLI-D-14-00458.1.

Scannell, H. A., A. J. Pershing, M. A. Alexander, A. C. Thomas, and K. E. Mills, 2016: Frequency of marine heatwaves in the North Atlantic and North Pacific since 1950. *Geophys. Res. Lett.*, **43**, 2069–2076, https://doi.org/10.1002/2015GL067308.

Sedlar, J., and A. Devasthale, 2012: Clear-sky thermodynamic and radiative anomalies over a sea ice sensitive region of the Arctic. *J. Geophys. Res.*, **117**, D19111, https://doi.org/10.1029/2012JD017754.

Seo, M., H.-C. Kim, K.-S. Lee, N.-H. Seong, E. Lee, J. Kim, and K.-S. Han, 2020: Characteristics of the reanalysis and satellite-based surface net radiation data in the Arctic. *J. Sens.*, **2020**, 1–13, https://doi.org/10.1155/2020/8825870.

Shupe, M. D., and J. M. Intrieri, 2004: Cloud radiative forcing of the Arctic surface: The influence of cloud properties, surface albedo, and solar zenith angle. *J. Climate*, **17**, 616–628, https://doi.org/10.1175/1520-0442(2004)017<0616:CRFOTA>2.0.CO;2.

Siddon, E. C., S. G. Zador, and G. L. Hunt Jr., 2020: Ecological responses to climate perturbations and minimal sea ice in the northern Bering Sea. *Deep-Sea Res. II*, **181–182**, 104914, https://doi.org/10.1016/j.dsr2.2020.104914.

Stabeno, P. J., and S. W. Bell, 2019: Extreme conditions in the Bering Sea (2017–2018): Record-breaking low sea-ice extent. *Geophys. Res. Lett.*, **46**, 8952–8959, https://doi.org/10.1029/2019GL083816.

——, J. D. Schumacher, and K. Ohtani, 1999: The physical oceanography of the Bering Sea: A summary of physical, chemical, and biological characteristics, and a synopsis of research on the Bering Sea. *Dynamics of the Bering Sea: A Summary of Physical, Chemical, and Biological Characteristics, and a Synopsis of Research on the Bering Sea*, T. R. Loughlin and K. Ohtani, Eds., North Pacific Marine Science Organization (PICES), 1–28.

——, N. A. Bond, and S. A. Salo, 2007: On the recent warming of the southeastern Bering Sea shelf. *Deep-Sea Res. II*, **54**, 2599–2618, https://doi.org/10.1016/j.dsr2.2007.08.023.

Suryan, R. M., and Coauthors, 2021: Ecosystem response persists after a prolonged marine heatwave. *Sci. Rep.*, **11**, 6235, https://doi.org/10.1038/s41598-021-83818-5.

Szuwalski, C. S., K. Aydin, E. J. Fedewa, B. Garber-Yonts, and M. A. Litzow, 2023: The collapse of eastern Bering Sea snow crab. *Science*, **382**, 306–310, https://doi.org/10.1126/science.adf6035.

Tanimoto, Y., H. Nakamura, T. Kagimoto, and S. Yamane, 2003: An active role of extratropical sea surface temperature anomalies in determining anomalous turbulent heat flux. *J. Geophys. Res.*, **108**, 3304, https://doi.org/10.1029/2002JC001750.

Thyng, K. M., C. A. Greene, R. D. Hetland, H. M. Zimmerle, and S. F. DiMarco, 2016: True colors of oceanography: Guidelines for effective and accurate colormap selection. *Oceanography*, **29** (3), 9–13, https://doi.org/10.5670/oceanog.2016.66.

Tian, F., and R.-H. Zhang, 2023: Increasing shortwave penetration through the bottom of the oceanic mixed layer in a warmer climate. *J. Geophys. Res. Oceans*, **128**, e2022JC019587, https://doi.org/10.1029/2022JC019587.

Wallace, J. M., C. Smith, and Q. Jiang, 1990: Spatial patterns of atmosphere-ocean interaction in the northern winter. *J. Climate*, **3**, 990–998, https://doi.org/10.1175/1520-0442(1990)003<0990:SPOAOI>2.0.CO;2.

Wang, J., H.-M. Kim, and E. K. M. Chang, 2017: Changes in Northern Hemisphere winter storm tracks under the background of Arctic amplification. *J. Climate*, **30**, 3705–3724, https://doi.org/10.1175/JCLI-D-16-0650.1.

Wirts, A. E., and G. C. Johnson, 2005: Recent interannual upper ocean variability in the deep southeastern Bering Sea. *J. Mar. Res.*, **63**, 381–405.

Woollings, T., and Coauthors, 2018: Blocking and its response to climate change. *Curr. Climate Change Rep.*, **4**, 287–300, https://doi.org/10.1007/s40641-018-0108-z.

Wooster, W. S., and A. B. Hollowed, 1995: Decadal-scale variations in the eastern subarctic Pacific: 1. Winter ocean conditions. *Can. Spec. Publ. Fish. Aquat. Sci.*, **121**, 81–85.

Wyatt, A. M., L. Resplandy, and A. Marchetti, 2022: Ecosystem impacts of marine heat waves in the northeast Pacific. *Biogeosciences*, **19**, 5689–5705, https://doi.org/10.5194/bg-19-5689-2022.

Yang, X.-Y., G. Wang, and N. Keenlyside, 2020: The Arctic sea ice extent change connected to Pacific decadal variability. *Cryosphere*, **14**, 693–708, https://doi.org/10.5194/tc-14-693-2020.

Brought to you by OREGON STATE UNIVERSITY | Unauthenticated | Downloaded 07/15/25 06:23 PM UTC